Structure – function studies of the membrane proteins involved in human iron metabolism

Menega Ganasen

Leading Program in Doctoral Education
Laboratory of Cellular Regulation
Graduate School of Life Science
University of Hyogo

December 2018

Contents

List of Publication

Parts of this thesis have been published in the following paper

Chapter 2

Structural basis for promotion of duodenal iron absorption by enteric ferric reductase with ascorbate

Menega Ganasen, Hiromi Togashi, Hanae Takeda, Honami Asakura, Takehiko Tosha, Keitaro Yamashita, Kunio Hirata, Yuko Nariai, Takeshi Urano, Xiaojing Yuan, Iqbal Hamza, A. Grant Mauk, Yoshitsugu Shiro, Hiroshi Sugimoto and Hitomi Sawai *Communications Biology*, **1** (2018) Article number 120

List of Presentations

Characterization of a novel heme transporter in animals

University of Hyogo & Universiti Putra Malaysia Joint Symposium. Oct 2015. Hyogo, Japan.

Menega Ganasen, Hitomi Sawai, Iqbal Hamza and Yoshitsugu Shiro

Characterization of a novel heme transporter in animals

BMB2015 Biochemistry and Molecular Biology. Nov 2015. Kobe, Japan.

Menega Ganasen, Hitomi Sawai, Iqbal Hamza and Yoshitsugu Shiro

Structural analysis of human duodenal cytochrome *b*561

The 89th Annual Meeting of Japanese Biochemical Society. Sep 2016. Sendai, Japan

Menega Ganasen, Hitomi Sawai, Yoshitsugu Shiro and Hiroshi Sugimoto

Structural insights into iron absorption mechanism in human duodenum by a membrane protein, Dcyt*b*

University of Strasbourg-RIKEN workshop on Membrane Lipidology. Mar 2017. Strasbourg, France.

Menega Ganasen, Hiroshi Sugimoto, Yoshitsugu Shiro and Hitomi Sawai

Structural insights into ascorbate-dependent ferrireductase, Dcyt*b*, in human

7th Congress of the International Bioiron Society. May 2017. Los Angeles, California

Menega Ganasen, Hitomi Sawai, Hiromi Togashi, Hanae Takeda, Yoshitsugu Shiro and Hiroshi Sugimoto

Structural analysis of a human duodenal ferrireductase, Dcyt*b*

The 17th Annual Meeting of the Protein Science Society of Japan. Jun 2017. Sendai, Japan

Menega Ganasen, Hitomi Sawai, Satoru Nagatoishi, Hiromi Togashi, Hanae Takeda, Kouhei Tsumoto, Yoshitsugu Shiro and Hiroshi Sugimoto

Structural insight into the dietary non-heme iron absorption in human duodenum

The 18th Annual Meeting of the Protein Science Society of Japan. Jun 2018. Niigata, Japan.

Menega Ganasen, Honami Asakura, Takehiko Tosha, Xiaojing Yuan, Iqbal Hamza, A. Grant Mauk, Yoshitsugu Shiro, Hiroshi Sugimoto and Hitomi Sawai

Understanding the mechanism of dietary iron absorption at the atomic level

The 91st Annual Meeting of Japanese Biochemical Society. Sep 2018. Kyoto, Japan.

Menega Ganasen, Honami Asakura, Takehiko Tosha, Takeshi Urano, Xiaojing Yuan, Iqbal Hamza, A. Grant Mauk, Yoshitsugu Shiro, Hiroshi Sugimoto and Hitomi Sawai

List of Awards

Young Poster Award

The 18th Annual Meeting of the Protein Science Society of Japan. Jun 2018. Niigata, Japan.

Young Scientist Award

The 91st Annual Meeting of Japanese Biochemical Society. Sep 2018. Kyoto, Japan.

Chapter 1: General introduction

Iron was believed to have therapeutic value as early as 1,500 BCE though few early uses for such treatment are now regarded as rational. Modern therapeutic use of orally administered iron was introduced by the English physician Thomas Sydenham (1624-1689) in the 17th century for the treatment of chlorosis (now known as iron deficiency anemia) with "iron tonic" (iron filings solubilized by tannins in wine), several years before the presence of iron in blood was demonstrated (Lemery and Geoffroy, 1713) and before consumption of iron was shown to increase the iron content of blood (Menghini, 1746). The extensive history of iron in medical practice has been reviewed elsewhere[1,2]. Today iron is recognized as an essential nutrient that is consumed by human beings in a sufficient amount as part of daily balanced diet. It serves as cofactors for many enzymes and proteins necessary for numerous biological functions such as oxygen transport, energy production and synthesis/metabolism of many bio-compounds, all of which are physiologically indispensable reactions for human[3]. Despite all these uses, iron can still be lethal to human if it is present less or more than the required amount. Iron deficiency is the most severe and widespread nutritional deficiency disorder that continues to affect more than 3.5 billion people of the world population[4] and remains the only nutritional deficiency disorder in industrialized countries[5,6]. On the other hand, iron overload causes accumulation of iron in various tissues and can result in cirrhosis[7], neurodegenerative and cardiovascular diseases (cardiomyopathy, *etc.*)[8,9] that result from formation of reactive oxygen species (ROS) through Fenton or Haber-Weiss reactions[10]. These pathological processes are normally prevented through strict regulation of iron uptake, storage and distribution because there is no regulated route of iron excretion.

The average iron level in a healthy human adult is 3 - 4 g. This level is maintained by three regulated processes in human, iron utilization in bone marrow for the synthesis of red blood cell, iron storage in liver in the form of ferritin and iron recycling from senescence red blood cells in

splenic macrophage. Despite that, 1-2 mg of iron is absorbed and loss every day to maintain the systemic iron balance (Figure 1-1)[11].

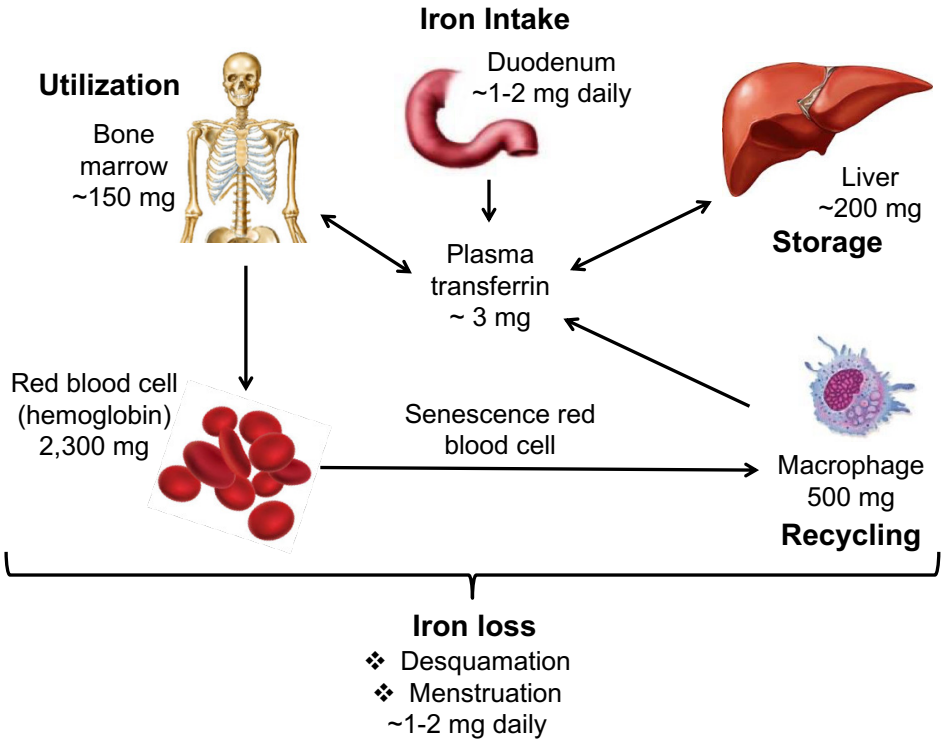

Figure 1-1. Iron homeostasis in human. Iron balance in human is maintained by strict regulation of iron intake, utilization, storage and recycling.

The average adult possesses 50 mg per kg of body weight of iron that is obtained from the diet in two forms, heme (Fe-protoporphyrin IX) and non-heme iron. Heme iron is derived from the hemoglobin and myoglobin present in red meat. It is more readily absorbed (12-25% bioavailable) and accounts for 10% of daily dietary iron intake. Non-heme iron refers to various forms of inorganic iron and is usually derived from plants and iron fortified food. It is poorly absorbed (<5% available) and accounts for 90% of daily dietary iron intake[12]. Dietary iron absorption is important not only to fulfill the intrinsic iron requirement of enterocyte for controlled regulation of systemic and cellular iron homeostasis, but also to balance the daily loss of iron. The failure to compensate this loss is the primary cause of iron deficiency anemia. To date, the dietary absorption of heme and non-heme iron in human body is far from being understood due to the lack of structural information on proteins involved in such regulation. In

this thesis, I have discussed the structure-function relationship of three proteins involved in dietary iron absorption: the product of Heme Responsive Gene (HRG) which is involved in heme iron absorption, and Duodenal Cytochrome *b* (Dcyt*b*) and Divalent Metal Transporter-1 (DMT-1) which are involved in non-heme iron absorption (Figure 1-2).

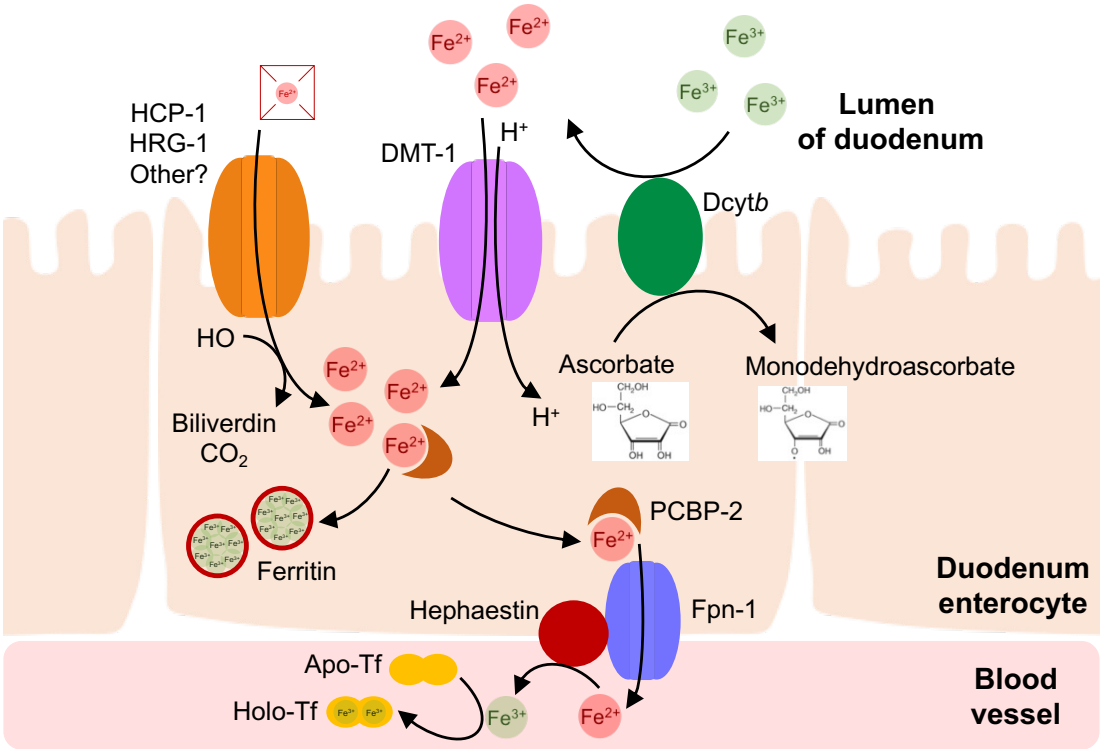

Figure 1-2. Heme and non-heme iron absorption in duodenal enterocyte. Heme and non-heme iron from diet are absorbed via different pathways. The imported Fe^{2+} is bound to PCBP-2, a Fe^{2+} chaperone. This is then either stored in the form of ferritin (Fe^{3+}) or transported into the blood by ferroportin-1 (Fpn-1). Fe^{2+} in blood is oxidized back to Fe^{3+} by hephaestin and carried to other parts of cell in transferrin (Tf) bound form.

In my PhD study, I characterized HRG-4 protein, which is the sole dietary heme transporter in *Caenorhabditis elegans*, a heme auxotroph. This is a homolog of HRG-1 protein in human, which is either expressed in duodenal enterocyte (for the uptake of dietary heme) or lysosomal membrane of macrophage (for the transport of heme out of phagolysosome after the lysis of senescence red blood cell). To further understand the human nutritional iron intake, I studied the molecular mechanism of Dcyt*b* and its possible interaction with DMT-1, which are both expressed in the brush border membrane of duodenal enterocyte in human.

References

1. Beutler, E. History of iron in medicine. *Blood Cells Mol. Dis.* **29**, 297-308 (2002).

2. Sheftel, A. D., Mason, A. B. & Ponka, P. The long history of iron in the Universe and in health and disease. *Biochim. Biophys. Acta* **1820**, 161-187 (2012).

3. Andrews, N. C. Iron homeostasis: insights from genetics and animal models. *Nat. Rev. Genet.* **1**, 208-217 (2000).

4. W. H. O. (WHO), Anaemia policy brief. Global Nutrition Targets **2025**, *working papers of WHO* (2016).

5. Stoltzfus, R. J. Iron deficiency: Global prevalence and consequences. *Food Nutr. Bull.* **24**, S99-103 (2003).

6. Baltussen, R., Knai, C. & Sharan, M. Iron fortification and iron supplementation are cost-effective interventions to reduce iron deficiency in four subregions of the world. *J. Nutr.* **134**, 2678-2684 (2004).

7. Fanni, D., *et al.* Effects of iron and copper overload on the human liver: An ultrastructural study. *Curr. Med. Chem.* **21**, 3768-3774 (2014).

8. Collingwood, J. F. & Davidson, M. R. The role of iron in neurodegenerative disorders: Insights and opportunities with synchrotron light. *Front. Pharmacol.* **5**, 191 (2014).

9. Baksi, A. J. & Pennell, D. J. Randomized controlled trials of iron chelators for the treatment of cardiac siderosis in thalassaemia major. *Front. Pharmacol.* **5**, 217 (2014).

10. Kehrer, J. P. The Haber-Weiss reaction and mechanisms of toxicity. *Toxicology* **149**, 43-50 (2000).

11. Abramowski, S. W., *et al.* Physiology of iron metabolism. *Transfus. Med. Hemother.* **41**, 213-221 (2014).

12. Bailey, R. L., West, K. P., Jr. & Black, R. E. The epidemiology of global micronutrient deficiencies. *Ann. Nutr. Metab.* **2**, 22-33 (2015).

Chapter 2: Characterization of a novel heme transporter in animals

2-1 Introduction

Heme, iron (Fe) protoporphyrin IX, covers a large portion of iron in all organisms, and it is employed as prosthetic group in many essential enzymes that participate in important biological processes. Heme is an efficient source of iron in diet, that has high bioavailability and easily absorbed[1,2]. Although heme biosynthesis and its regulation have been extensively studied, very little is known about heme trafficking or heme absorption. Heme readily diffuses through the lipid bilayers due to the hydrophobicity of the porphyrin ring. However, the exit of heme across the lipid bilayer is somehow impossible. Because of the hydrophilic property of propionate head groups, this hinders the flipping of heme from one leaflet to another[3]. Therefore, the heme exit from the membrane is unattainable without the presence of heme transporters in the membrane[4]. In mammals, Heme Carrier Protein-1 (HCP-1) is the first heme transporter that was identified to be expressed in the apical membrane of duodenal enterocyte. It was isolated from mouse duodenum, localized to the plasma membrane. The heme uptake was analysed by functional studies using *Xenopus* oocytes[5]. However, recent studies showed that HCP-1 has low-affinity to heme and it is more involved in folate absorption[6]. The identity of dietary heme transporter remained elusive until the discovery of Heme Responsive Gene (HRG) protein.

HRG was first discovered by exploiting the well-defined genetics of *Caenorhabditis*, a free living worm, which is a natural heme auxotroph. This worm lacks of all required genes to synthesize heme and solely depends on dietary heme to sustain its growth and development. *Caenorhabditis elegans* Heme Responsive Gene-1 (*Ce*HRG-1) and *Caenorhabditis elegans* Heme Responsive Gene-4 (*Ce*HRG-4) were the first heme transporters identified from this species. These proteins were initially discovered as transmembrane permeases upregulated in response to heme deficiency. Both proteins are expressed in the worm intestine with *Ce*HRG-1 localized within an intracellular vesicular compartment and *Ce*HRG-4 localized to the apical plasma membrane (Figure 2-1).

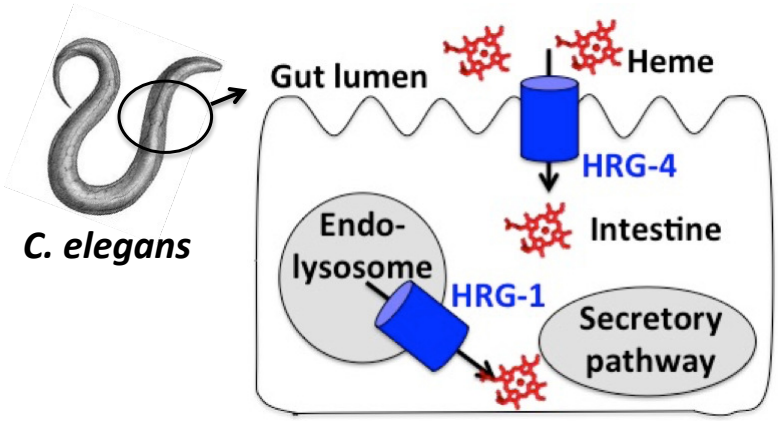

Figure 2-1. Intracellular heme trafficking system in *C. elegans*. HRG-1 is localized in endolysosomal membrane, whereas HRG-4 is localized in the apical plasma membrane.

An interesting fact about HRG proteins is that these proteins are broadly conserved in animals and in human[7]. In human, HRG-1 expression was first identified in the phagolysosomal membrane of splenic macrophage, where it transports heme from the phagolysosome to the cytoplasm during erythrophagocytosis (Figure 2-2). The cytoplasm of erythrocytes is rich in hemoglobin, a molecule with four iron containing heme groups. During erythrophagocytosis, the senescence red blood cells (sRBC) are lysed in the acidic environment of the endophagolysosome. A massive amount of heme is released from this process and exit from phagolysosome via HRG-1. Heme oxygenase-1 then degrades the heme to release the iron[8]. Apart from this, HRG-1 is also hypothesized to be important in the absorption of dietary heme by duodenal enterocyte[2].

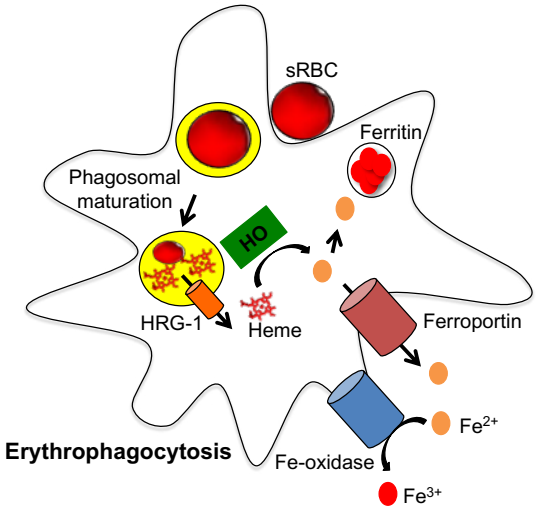

Figure 2-2. Heme trafficking in erythrophagocytosis process. Heme released for the breakdown of senescence red blood cells is transported out of phagolysosome by HRG-1.

While HRG-1 had been found in diverse organisms including humans, *Ce*HRG-4 appears only in heme auxotrophs such as roundworms, parasitic helminths, and some protozoan parasites[7,9]. The heme auxotrophs must acquire heme using *Ce*HRG-4 from the environment to survive. Helminths and protozoan parasites affect more than a quarter of the world's population[10] and cause tens of billions of dollars of loss in animal and plant production annually[11]. Therefore, elucidations of the heme transport mechanism by *Ce*HRG-4 and control of its function will be expected to be a benchmark for the development of antihelminthics and anti-parasitic drugs. The study on *Ce*HRG-4 will also provide understanding on human HRG transporters, as these proteins are broadly conserved. Following that, the objective of this study is to understand the heme trafficking by *Ce*HRG-4 by using structural and functional studies.

2-2 Material and methods

2-2-1 Protein expression and membrane preparation

An artificially synthesized *Ce*HRG-4 gene that includes *C*-terminal Strep tag II was cloned into the pPICZ C vector (Invitrogen) for expression in *Pichia pastoris*. Cells were grown in BMGY medium containing 1% (w/v) yeast extract, 2% (w/v) peptone, 0.1 M potassium phosphate buffer, 1.34% (w/v) yeast nitrogen base, 0.002% (w/v) biotin and 1% (w/v) glycerol. Overexpression of *Ce*HRG-4 was induced by the addition of 1% methanol. Cells were harvested after 30 h of culture growth at 30°C. The harvested cells (~ 80 g) were resuspended in lysis buffer (~ 200 mL) containing 20 mM Tris-HCl (pH 7.4), 200 mM NaCl, 20% (w/v) glycerol and one tablet of cOmplete EDTA-free protease inhibitor cocktail (Roche) followed by disruption by bead beater using zirconia beads (equal volume with lysis buffer) for 9 min ((1 min disruption + 3 min interval on ice) – repeat 9 times). Cell debris was removed by centrifugation (9,000 × *g* for 20 min with an R13A angle rotor and CR22N centrifuge (Hitachi)). The supernatant fluid was collected and sedimented by ultracentrifugation (40,000 × *g* for 1 h with a P45AT angle rotor and

CP80WX ultracentrifuge (Hitachi)) to obtain the membrane fraction. Membrane fraction was then homogenized with lysis buffer.

2-2-2 Detergent screening and purification of *Ce*HRG-4

The solubilization and purification of *Ce*HRG-4 was optimized by detergent screening. List of the detergents used, and the concentration of detergents used for solubilization and purification is summarized in Table 2-1. The membrane fraction was diluted in solubilization buffer containing 20 mM Tris-HCl (pH 8), 150 mM NaCl, 10% (w/v) glycerol, 1 mM EDTA and 0.2 % (w/v) cholesteryl hemisuccinate (CHS) to a concentration of 5 mg/mL. The diluted membrane was then solubilized with respective detergent at concentration stated in Table 2-1, for 1 h at 4°C, with constant stirring. Following ultracentrifugation (40,000 rpm for 1 h), the supernatant fluid was diluted 10 times by solubilization buffer before loaded onto a column of streptavidin agarose affinity resin (Strep-tactin; IBA life science). Non-specifically bound material was eluted from this column with lysis washing buffer containing 20 mM Tris-HCl (pH 8), 150 mM NaCl, 10% (w/v) glycerol, 1 mM EDTA, 0.01 % (w/v) CHS and respective detergent, and the solubilized *Ce*HRG-4 was eluted by the same buffer containing 3 mM d-Desthiobiotin (Sigma-Aldrich). Purification profile was evaluated by SDS-PAGE (Invitrogen). The resulting protein from the elution fraction was concentrated up to ~500 μL and purified by gel filtration chromatography (HiLoad 13/30 Superdex 200 pg; GE Healthcare) in buffer containing 20 mM Tris-HCl (pH 7.4), 150 mM NaCl, 10% (w/v) glycerol 0.01 % (w/v) CHS and respective detergent. Based on the detergent screening, DDM was chosen for final purification for crystallization, using the purification protocol stated above. The oligomerization state of *Ce*HRG-4 was evaluated by blue native PAGE using NativePAGE Bis-Tris gel system (Invitrogen).

Table 2-1: List of detergent used for solubilization and purification

Detergent abbreviation	Detergent name	CMC* (%)	Solubilization Concentration	Purification Concentration
LDAO	n-Dodecyl-N,N-dimethylamine-N-oxide	0.023	0.48%	0.07%
C_8E_4	Tetraethylene glycol monoctyl ether	0.25	1.3%	0.5%
DM	n-Decyl-β-D-maltopyranoside	0.087	1%	0.26%
DDM	n-Dodecyl-β-D-maltopyranoside	0.0087	1%	0.05%
UDM	n-Undecyl-β-D-maltopyranoside	0.029	1%	0.087%
$C_{12}E_8$	Octaethylene monododecyl ether	0.0048	1%	0.014%
CHAPS		0.49	1.6%	0.61%
	Sodium Cholate	0.60	1.6%	0.8%

***Critical micelle concentration (CMC)** is the concentration of detergents above which micelles are spontaneously formed

2-2-3 Crystallization of *Ce*HRG-4

Highly purified *Ce*HRG-4 was concentrated and crystallized by vapor diffusion (sitting-drop) method and incubated at 20 °C and 4 °C. Few crystal hits obtained from crystallization screening by commercially available screening kits were picked and flash cooled by liquid nitrogen. These conditions were not optimized further because the crystals were not diffracted by X-rays.

2-2-4 *In vivo* yeast spot assay

The pYES-DEST52 (Thermo Fisher Scientific) carrying the *CeHRG-4* gene were transformed into *hem1*Δ *Saccharomyces cerevisiae* mutant. This mutant strain lacks the gene encoding aminolevulinic acid (ALA) synthase, which is the rate-limiting enzyme in the heme biosynthesis pathway. Prior to spotting, cells were cultivated in enriched synthetic complete (SC) medium without histidine, containing 2% w/v raffinose for 18 h to deplete heme. Cells were then suspended in water to an A600 of 0.2. 10 μL of 10-fold serial dilutions of each transformant was spotted onto 2% w/v raffinose SC (-His) plates supplemented with either 0.4% (w/v) glucose (suppress the protein expression) and 250 μM ALA (positive control), or 0.4% (w/v) galactose (induce the protein expression) and different concentrations of hemin (1, 3 and 10 μM) or different concentration of protoporphyrin IX (PPIX) (1, 3 and 10 μM). Plates were incubated at 30 °C for 3 days before imaging.

2-3 Results

2-3-1 Expression and purification of *Ce*HRG-4

Recombinant *Ce*HRG-4 was overexpressed in *Pichia pastoris*. The expression of *Ce*HRG-4 was confirmed by western blot with anti-strep tag II antibody (Figure 2-3), and the protein purification by affinity and gel filtration chromatography were optimized by detergent screening (Figure 2-4 & 2-5). High yield of purification was observed after affinity chromatography by using DDM, UDM and $C_{12}E_8$ detergents. However, the oligomerization state was observed to differ drastically for each detergent from gel filtration chromatography.

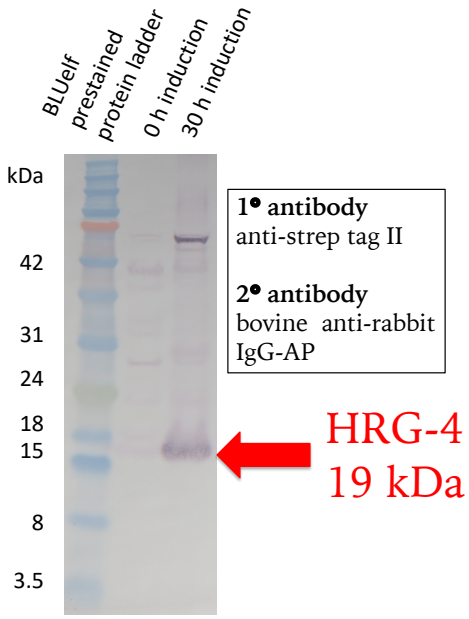

Figure 2-3. Western blot analysis of *Ce*HRG-4, expressed in yeast. 25.0 µg protein was loaded per lane, and expressed protein was detected by anti-strep tag II.

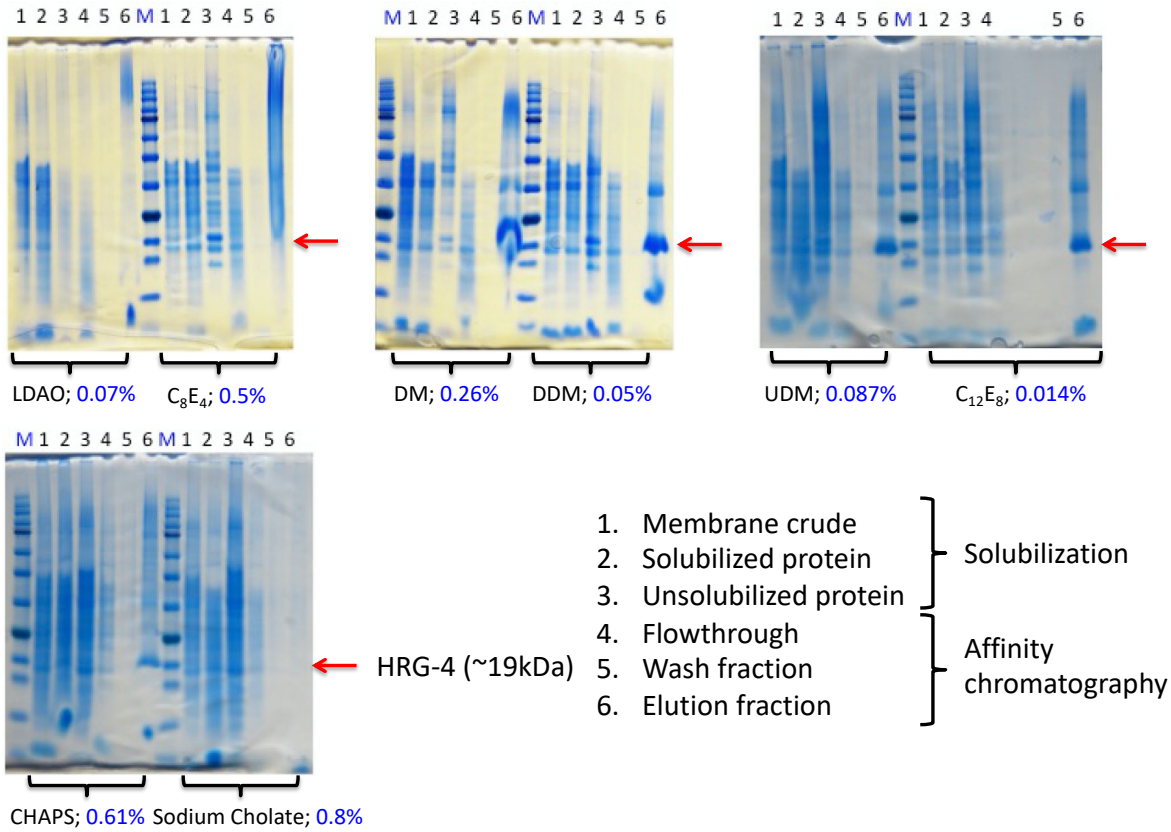

Figure 2-4. SDS-PAGE profile for detergent screening in affinity chromatography. *Ce*HRG-4 obtained from solubilization and affinity chromatography was analyzed by SDS-PAGE. Better yield of purified protein was obtained using DDM, UDM, $C_{12}E_8$ and CHAPS, in that order.

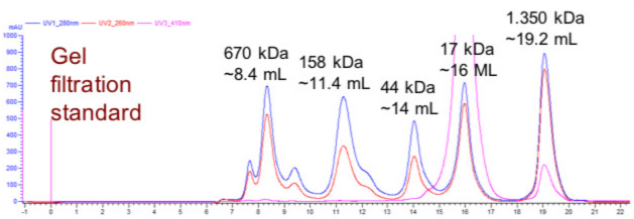

Gel filtration standard (Bio-Rad)	
Component	Molecular weight (kDa)
Thyroglobulin (bovine)	670
γ – globulin (bovine)	158
Ovalbumin (chicken)	44
Myoglobin (horse)	17
Vitamin B_{12}	1.35

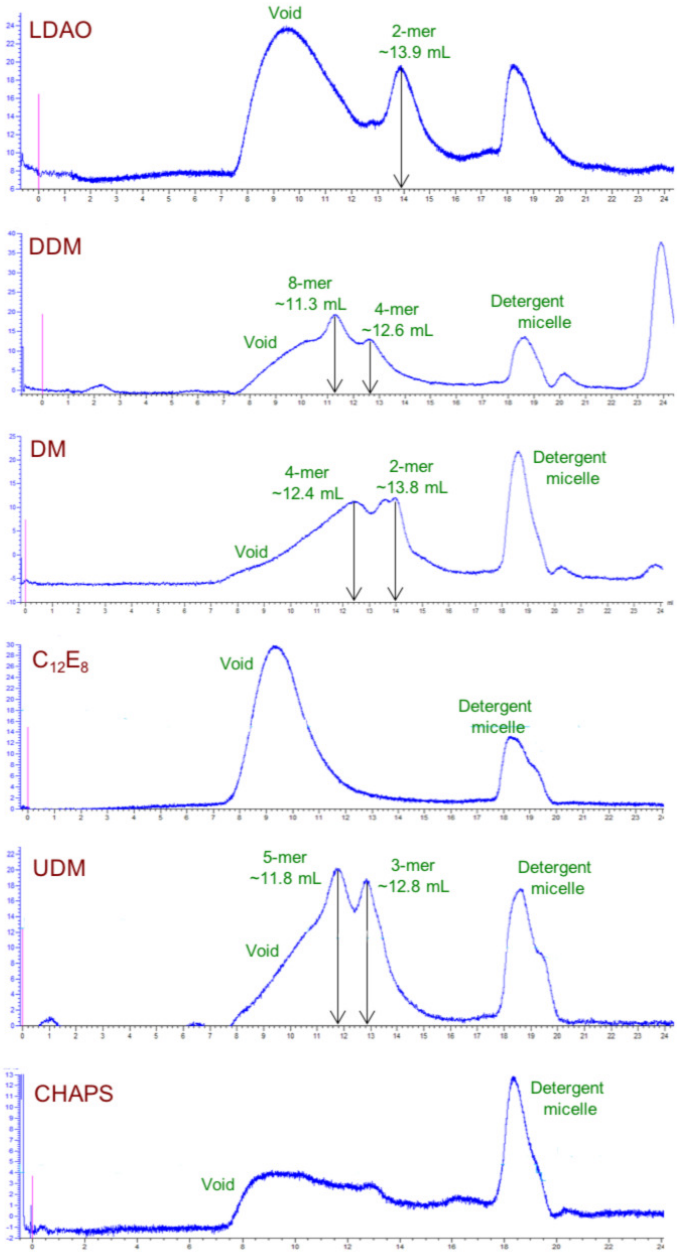

Figure 2-5. Gel filtration profile for *Ce*HRG-4 under various detergents. The number of oligomers of *Ce*HRG-4 under each detergent was determined by comparing the peak position with gel filtration standard.

DDM was chosen as the final choice for solubilization and purification, and *Ce*HRG-4 was purified by affinity and gel filtration chromatography, in the presence of DDM and CHS (Figure 2-6). Two peaks were observed from the gel filtration profile, peak 1 is the void volume and peak 2 is 8-mer of HRG-4.

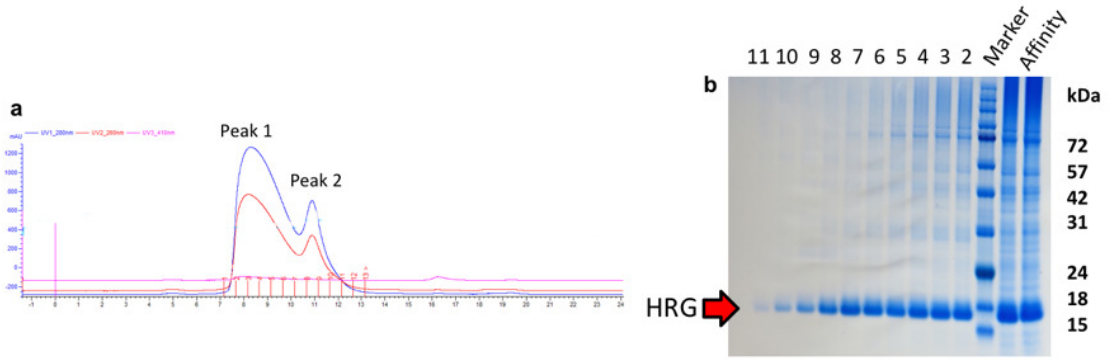

Figure 2-6. Protein purification profile. a. Purification chromatogram from gel filtration chromatography. The red and blue line represent absorbance at $A_{260\,nm}$ and $A_{280\,nm}$, respectively **b.** 10% SDS-PAGE of purified *Ce*HRG-4.

Sample from affinity chromatography and two peak fractions from gel filtration chromatography were used for blue native page to analyse the oligomerization state of *Ce*HRG-4. Two visible bands appeared in native page (Figure 2-7). The lower band at ~40 kDa might correspond to the detergent micelle, whereas the top band at ~146 kDa might correspond to *Ce*HRG-4 8-mer.

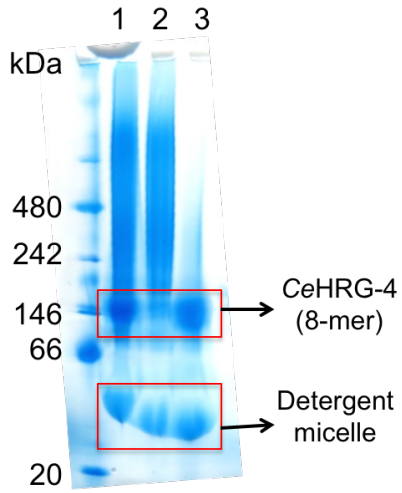

Figure 2-7. Blue Native PAGE analysis of *Ce*HRG-4. Lane 1, 2 and 3 corresponds to sample from gel filtration peak 1 (30 μM), gel filtration peak 2 (10 μM) and affinity chromatography (30 μM), respectively.

2-3-2 Initial crystallization screening of *Ce*HRG-4

Potential hits in the initial crystallization screening of *Ce*HRG-4 were obtained only in a few conditions from 384 conditions of commercially available crystal screening kits (Figure 2-8). The sample in the drop were picked and flash cooled in liquid nitrogen. No diffraction spots were observed for any of these sample at BL32XU of SPring-8.

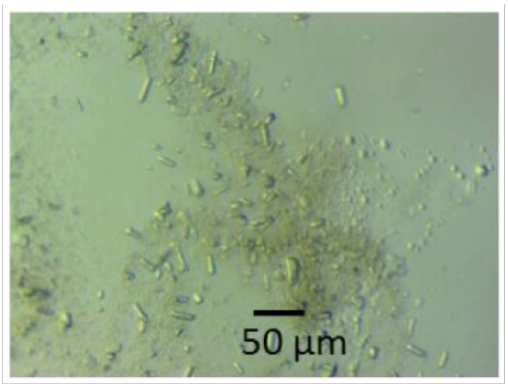

Protein concentration: ~4 mg/mL

MemMeso
0.1 M NaCl
0.1 M MES (pH 6.0)
0.1 M $MgCl_2$
30% (v/v) PEG300

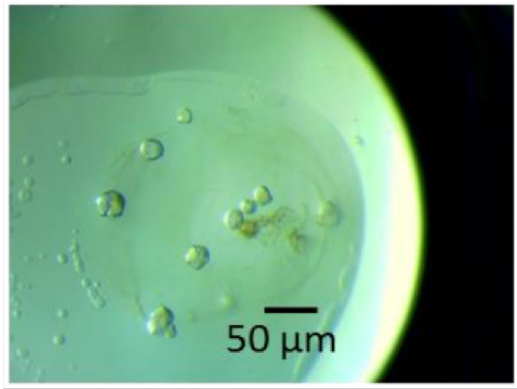

Protein concentration: ~10 mg/mL

Morpheus II
100 mM Monosaccharides II
0.1 M Buffer System 4
(1 M MOPSO, Bis-Tris pH 6.5)
50% v/v Precipitant Mix 5

Figure 2-8. Initial crystallization screening of *Ce*HRG-4. The sitting drops of *Ce*HRG-4 were equilibrated by vapour diffusion (0.1 µL protein solution + 0.1 µL precipitant solution) at 20°C.

2-3-3 *In vivo* yeast spot assay

Notably, transformants *hem1*Δ *S. cerevisiae* expressed *Ce*HRG-4 expression showed positive and significant growth, at increasing concentration of hemin and protoporphyrin (PPIX), with better growth in hemin than PPIX. On the other hand *hem1*Δ *S. cerevisiae* strain transformed with vector showed slight growth only at high concentration of hemin and PPIX (10 µM), with better growth in PPIX compared to hemin. The accumulation of red pigment was observed in *Ce*HRG-4 transformed strain at high hemin concentration (10 µM), and no pigmentation was observed in vector transformed strain (Figure 2-9). The red pigmentation is caused by the mutation in *ade2* gene, that is present in the *hem1*Δ genetic background[12,13]. This mutant

accumulate phosphoribosylaminoimidazole, an intermediate in the adenine biosynthesis pathway, and this turns red in the presence of oxygen[14]. Therefore, high pigment accumulation in *Ce*HRG-4 transformed is a sign that oxidative phosphorylation or mitochondrial respiration was restored in this heme-deficient mutant, by hemin source and not by PPIX source.

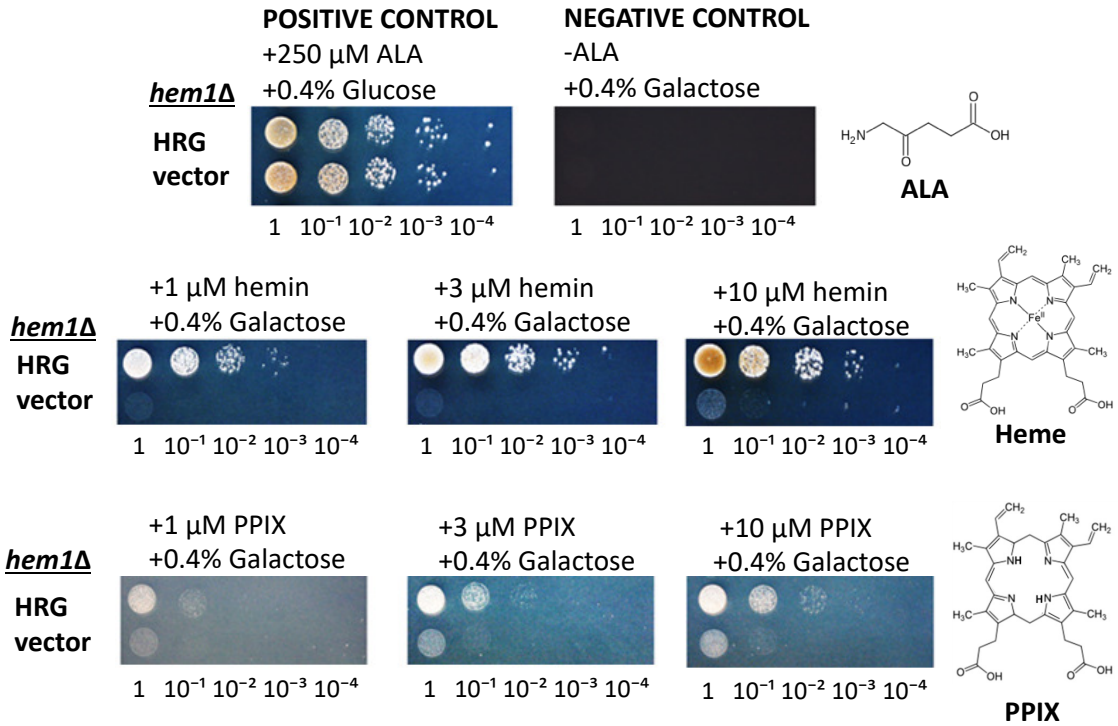

Figure 2-9. *In vivo* yeast spot assay for *Ce*HRG-4 and vector transformed heme deficient *S. cerevisiae* mutant. The *hem1*Δ *S. cerevisiae* mutant strain transformed with the indicated constructs were spotted in 10-fold serial dilution.

2-4 Discussion

As a heme auxotroph, *C. elegans* solely depends on dietary heme source for its survival. *Ce*HRG-4 was identified as the only heme transporter that transports extracellular heme into the intestinal cytoplasm. Understanding the mechanism of heme trafficking by membrane protein transporter at atomic level is an interesting issue that still remains unresolved due to no structural information available for any heme transporter.

The main aim of this study was to structurally characterize *Ce*HRG-4. Although the protein was successfully purified, no promising crystals were obtained from crystallization screening. In membrane protein research, one of the most important step is the choice of best detergent that maintain the target membrane protein in a functional, folded state in the absence of membrane[15]. This was a big challenge in *Ce*HRG-4 purification and crystallization. Based on the comparison between gel filtration standard and the gel filtration chromatography profile of *Ce*HRG-4 under different detergents, the protein was found to acquire various numbers of oligomers, ranging from dimer to 8-mer, and most of the protein were eluted in the void fraction. Since the actual oligomerization state of *Ce*HRG-4 is not known, this property could not be used to evaluate the choice of detergent. Choice of detergent was finally made from the protein yield and detergent critical micelle concentration (CMC). A larger detergent CMC is not suitable for crystallization as the detergent micelles will interrupt crystal packing. Following that, DDM was used for solubilization and purification of *Ce*HRG-4. The crystallization of *Ce*HRG-4 remains a challenge even with optimized detergent conditions. The success of crystal structure depends on the unique and tight arrangement of protein molecules in the crystalline liquid. Homogeneity of purified protein and space between each molecules are important factors that determines this packing. Both this factors are highly affected in the purified *Ce*HRG-4 due to the presence of detergent micelle.

An interesting finding from the current study is the hemin and PPIX transport assay using heme deficient *S. cerevisiae* mutant. A previous study on *Ce*HRG-4 proposed a mechanistic model for heme import trafficking route using mutagenesis and functional assay. By using the topological model of *Ce*HRG-4, they found a few conserved Histidine residues, which are predicted as heme ligand or heme interacting site, and these residues are shown to be conserved among other HRG proteins. H108 is one of main residue, which is placed on the external loop of the non-cytoplasmic side (Figure 2-10), that probably binds to the heme at the metal centre and initiate the heme transport[9]. However, the ability of *Ce*HRG-4 to transport PPIX shows that this protein possibly identifies heme by the porphyrin ring in addition to the metal centre.

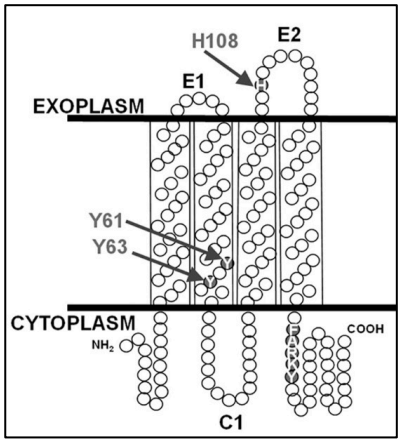

Figure 2-10: Putative topological model of *Ce*HRG-4 adapted from Yuan *et al.*, 2011. The shaded residues were predicted as potential heme interacting residues. H108 was known as main residue involved in triggering the heme transport through heme interaction

2-5 Conclusion

In summary, the role of *Ce*HRG-4 in heme transport is partly understood from the *in vivo* yeast spot assay. *Ce*HRG-4 is also able to transport PPIX in addition to heme. The mechanism of heme transport and the heme binding or interaction site is still unknown, and further investigation is required to clearly understand the role of *Ce*HRG-4 in heme transport. With the advancing field of X-ray crystallography and electron microscopy, the problematic structural determination of HRG proteins could be tackled in near future.

2-6 References

1. Latunde-Dada, G. O., Simpson, R. J. & McKie A. T. Recent advances in mammalian haem transport. *Trends Biochem. Sci.* **31**, 182-188 (2006).

2. Staron, R., *et al*. Dietary haemoglobin rescues young piglets from severe iron deficiency anemia: Duodenal expression profile of genes involved in heme iron absorption. *PLoS ONE* **12(7)**, e0181117 (2017).

3. Light, W. R. III & Olson, J. S. Transmembrane movement of heme. *J. Biol. Chem.* **265**, 15623-15631 (1990).

4. Korolnek, T. & Hamza, I. Like iron in the blood of the people: the requirement for heme trafficking in iron metabolism. *Front. in Pharmacol.* **5**, 1-13 (2014).

5. McKie A. T., *et al.* A novel duodenal iron-regulated transporter, IREG1, implicated in the basolateral transfer of iron to the circulation. *Mol. Cell* **5**, 299-309 (2000).

6. Silva, B. & Faustino, P. An overview of molecular basis of iron metabolism regulation and the associated pathologies. *BBA* **1852**, 1347-1359 (2015)

7. Rajagopal, A., *et al.* Haem homeostasis is regulated by the conserved and concerted functions of HRG-1 proteins. *Nature* **453**, 1127-1131 (2008).

8. White, C., *et al.* HRG1 is essential for heme transport from the phagolysosome of macrophage during erythrophagocytosis *Cell Metab.* **17**, 261-270 (2013).

9. Yuan, X., Protchenko, O., Philpott, C. C. & Hamza, I. Topologically conserved residues direct heme transport in HRG-1-related proteins *J. Biol. Chem.* **287**, 4914-4924 (2012).

10. Chan, M. S., Medley, G. F., Jamison, D., & Bundy, D. A. The evaluation of potential global morbidity attributable to intestinal nematode infections. *Parasitology* **109**, 373-387 (1994).

11. Fuller, V. L., Lilley, C. J. & Urwin, P. E. Nematode resistance. *New Phytol.* 180: 27-44 (2008).

12. Crisp, R. J., *et al.* Inhibition of heme biosynthesis prevents transcription of iron uptake genes in yeast. *J. Biol. Chem.* **278**, 45499–45506 (2003).

13. Myers, A. M., Pape, L. K., & Tzagoloff, A. Mitochondrial protein synthesis is required for maintenance of intact mitochondrial genomes in *Saccharomyces cerevisiae*. *EMBO J.* **4**, 2087–2092 (1985).

14. Chen, C., Samuel, T. K., Krause, M., Dailey, H. A. & Hamza, I. Heme utilization in the *Caenorhabditis elegans* Hypodermal cells is facilitated by Heme-responsive Gene-2. *J. Biol. Chem.* **287**, 9601-9612 (2012).

15. Prive, G. G. Detergents for the stabilization and crystallization of membrane proteins. *Methods* **41**, 388-397 (2007).

Chapter 3 : Structural insights into non-heme iron absorption in human duodenum

3-1 Introduction

Non-heme iron represents the majority of iron consumed by humans in their diets. It is highly found in grains such as rice, wheat and oats, in nuts, fruits, vegetables, fortified foods and in most iron supplements. Moreover, 55-60% of iron found in meat is also non-heme iron. Human body absorb heme iron better than non-heme iron. This is one of the reasons why vegetarians are more at risk to develop iron deficiency anemia. The main cause for this is the unawareness about the importance and mechanism of non-heme dietary iron absorption.

Non-heme iron primarily occurs in its oxidized, water insoluble ferric form (Fe^{3+}). The absorption of non-heme iron has long been known with the discovery of Duodenal Cytochrome *b* (Dcyt*b*)[1] and Divalent Metal Transporter-1 (DMT-1)[2]. Dcyt*b* is membrane embedded iron-regulated Fe^{3+} reductase that was first identified in the duodenal brush border of mice with systemic iron deficiency[1]. As DMT-1 is selective for the absorption of iron in its ferrous form (Fe^{2+})[2], the reduction of Fe^{3+} to Fe^{2+} by Dcyt*b* in the duodenum is the key step for effective intestinal iron absorption (Figure 3-1).

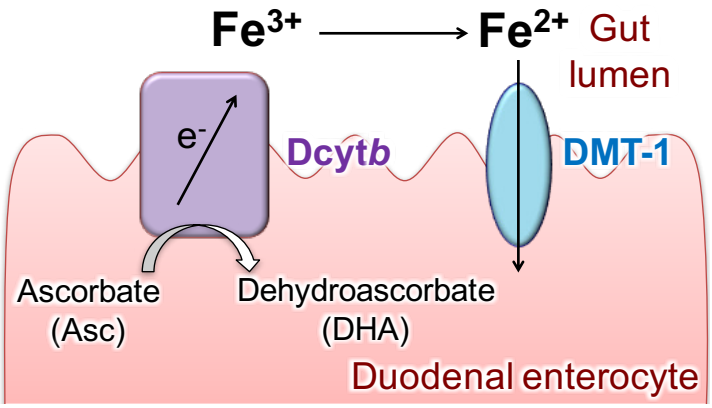

Figure 3-1. Non-heme iron absorption in duodenal enterocyte. Dietary iron is imported into duodenal enterocyte via DMT-1 following reduction by the transmembrane ferric reductase Dcyt*b*.

The importance of Dcyt*b* in iron homeostasis has been studied for a long time. Notably, the expression and activity of mucosal Dcyt*b* are closely associated with chronic anemia and

hypoxia[3]. Dcyt*b* utilizes ascorbate in cytoplasm as an electron donor to reduce apical Fe^{3+}. Human enteric ferric reductase Dcyt*b* is a member of the cytochrome b_{561} (Cytb_{561}) protein family, all of which are ascorbate-dependent oxidoreductases that are homo-dimeric, integral membrane proteins. Each monomer possesses six transmembrane helices and two heme *b* groups[4,5]. All members of this family use cytoplasmic ascorbate as an electron donor for the reduction of a substrate at the non-cytoplasmic side of the enzyme. The two heme *b* groups mediate intra-molecular electron-transfer reaction across the membrane.

The absorption of bioactive and water soluble Fe^{2+} is a challenge for all forms of life and left a great impact on evolution. This biological challenge has led to the identification and functional characterization of many ferric reductases. The most well studied metalloreductase is FRE family from yeast. FRE reduces siderophore-bound iron and oxidized copper prior to uptake by yeast metal transporters[6,7]. The ferric reductase in plants is known as ferric reductase oxidase (FRO) protein, which was first identified in *Arabidopsis*, as a protein that reduces Fe^{3+}-chelates at the root surface-rhizosphere interface[8,9]. Plants also possess a protein from Cytb_{561} family, however, the role of plant Cytb_{561} as Fe^{3+} reductase has not been fully established due to the existence of FRO protein as their principal Fe^{3+} reductase. Compared to yeast and plants, humans have two classes of ferric reductases, Dcyt*b* from Cytb_{561} family, and STEAP3 from the STEAP protein family, which is required for transferrin-dependent iron uptake and expressed as lysosomal membrane protein[10]. Dcyt*b* however, is the only iron-regulated ferric reductase that is required for optimal iron metabolism. It is likely to increase the bioavailability of Fe^{2+} for the transport by DMT-1 under iron limited condition in human body.

Following the importance of Dcyt*b* in human iron metabolism, the knowledge for the molecular mechanisms of the iron recognition, ferrireductase function and electron transfer on the Dcyt*b* is necessary to understand and eradicate the iron metabolism disorders. However, it has been hampered by the lack of atomic-level structural information of Dcyt*b*. This work provides the first crystal structure of Dcyt*b* in ascorbate and metal bound form. Biochemical and spectroscopic analysis combined with the structure-guided mutagenesis were also performed to

gain the functional insights of Dcyt*b*. Since ascorbate is known as a vitamin C cofactor to enhance dietary iron absorption[11,12], the effect of dietary Fe^{3+}-chelators on Dcyt*b* function was also investigated. These findings provide insights on how humans absorb non-heme iron at the atomic levels and another role of ascorbate and dietary iron-chelators for non-heme iron absorption that facilitates the development of new and effective oral ferrotherapy.

3-2 Material and methods

3-2-1 Expression and purification of Dcyt*b*

A codon-optimized gene encoding Dcyt*b* that includes a thrombin cleavage site followed by a *C*-terminal hexa-His tag was cloned into the pET-21b(+) vector (Merck Millipore) for expression in *Escherichia coli* BL21 Star(DE3) (Invitrogen). Transfected cells were grown in TB medium containing δ-aminolevulinic acid (ALA) (0.5 mM) and ampicillin (50 mg L^{-1}). Overexpression of Dcyt*b* was induced by isopropyl β-D-thiogalactoside (0.1 mM) when the culture achieved an OD_{600} of 1.5-1.7, and cell growth was continued for 18 h at 20°C. The harvested cells (~80 g) were suspended in phosphate buffered saline (pH 7.0) to a final volume of 120 mL. DNase I (10 mg/mL), lysozyme (20 mg/mL) and one tablet of cOmplete EDTA-free protease inhibitor cocktail (Roche) were added to this mixture, followed by disruption with a French press (Ohtake). Cell debris was removed by centrifugation (7,400 × *g* for 30 min with an R13A angle rotor and CR22N centrifuge (Hitachi)). The supernatant fluid was collected and sedimented by ultracentrifugation (66,000 × *g* for 1 h with a P45AT angle rotor and CP80WX ultracentrifuge (Hitachi)) to obtain the membrane fraction. This fraction was then homogenized with lysis buffer (Na_2HPO_4 (50 mM), citric acid (10 mM) and NaCl (150 mM), pH 5.8) and solubilized in a solution containing sodium deoxycholate (0.5% (w/v)) (Wako Pure Chemical) and n-dodecyl-β-D-maltopyranoside (DDM) (1.7% (w/v)) for 1 h at 4°C. Following ultracentrifugation (40,000 rpm for 1 h), the supernatant fluid was loaded onto a column of Ni^{2+}-

nitrilotriacetate affinity resin (Ni-NTA; Qiagen). Non-specifically bound material was eluted from this column with lysis buffer containing 10 mM imidazole (pH 5.8) (washing buffer), and the solubilized Dcyt*b* was eluted by the same buffer containing 500 mM imidazole (pH 5.8). The hexa-His tag was cleaved by overnight treatment with biotinylated thrombin (Merck Millipore) (2.5 units per 1 mg of protein) at 20°C, followed by the incubation of this reaction mixture with streptavidin agarose (Merck Millipore) (32 μL per 1 unit of biotinylated thrombin) for 1 h at 4 °C to capture the biotinylated thrombin. The resulting protein solution was loaded into Ni-NTA column once again, and the His-tag-cleaved Dcyt*b* was eluted with washing buffer. The resulting Dcyt*b* solution was concentrated to ~4-5 mg/mL by centrifugal ultrafiltration and purified by gel filtration chromatography (HiLoad 16/600 Superdex 200 pg; GE Healthcare) equilibrated with MES-Na buffer (50 mM, pH 6.5) containing NaCl (150 mM) and DDM (0.025%). The peak fractions were collected and concentrated (~15 mg/mL) for crystallization with a centrifugal ultrafiltration unit (Amicon, Merck Millipore) having a 50 kDa cutoff. The protein concentration was determined based on UV visible absorbance at $A_{414\ nm}$, where the protein concentration is 1 mg/mL when $A_{414\ nm} = 10.0$.

3-2-2 Crystallization of Dcyt*b*

Purified Dcyt*b* was crystallized by the lipidic cubic phase (LCP) method. This is a rising approach which allows the crystallization of membrane protein in native like environment[13,14]. Protein solution (~15 mg/mL) was mixed with monoolein (9.9 MAG; Nu-Chek Prep, Inc) at a 2:3 ratio (w/w) with a coupled syringe mixer. Samples (50 nL) of protein-laden LCP were dispensed onto a 96-well sandwich plate (Molecular Dimensions) and overlaid with precipitant solutions (0.8 μL) with a mosquito LCP device (TTP Labtech). Schematic representation of crystallization is shown in Figure 3-2. Initial crystallization hits were identified in the presence of 20% (v/v) Jeffamine ED-2003 and 0.1 M HEPES (pH 6.5). Crystallization conditions were optimized by screening further with buffer containing a series of Jeffamine concentrations and varying pH.

Crystals that reached full size (~4-8 μm) within two days at 20°C were harvested from the mesophase and were flash cooled in liquid nitrogen without additional cryoprotectant. Crystals of Dcyt*b* with substrate bound were obtained by soaking crystals grown for two weeks at 20°C with precipitant solution containing sodium ascorbate (1 M) and $ZnSO_4$ (10 mM) for 30 min and, finally, flash cooled in liquid nitrogen.

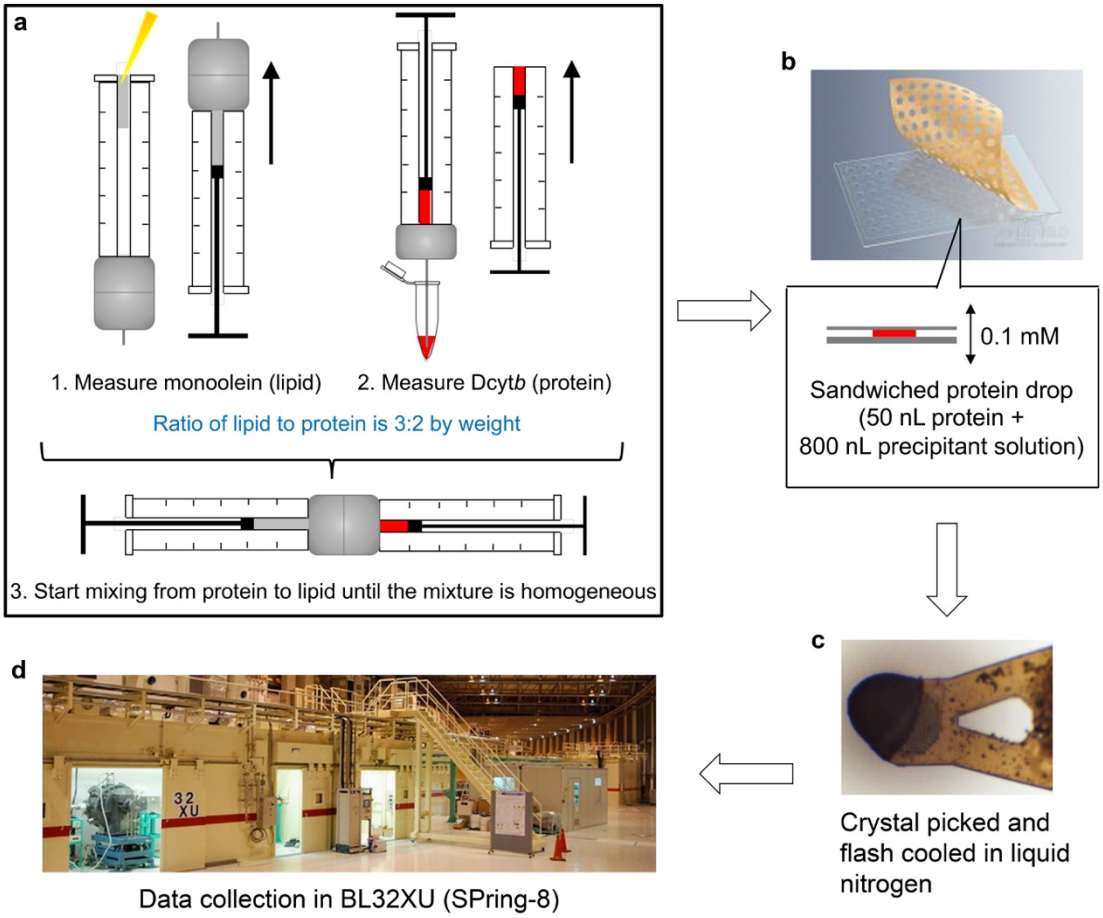

Figure 3-2. Schematic representation of crystallization protocol for Dcyt*b*. a. Preparation of Dcyt*b* in lipidic cubic phase. **b.** Protein drop sandwiched in LCP plate after crystallization setup by mosquito. **c.** LCP drop with full grown crystals are picked by mesh and flashed cooled in liquid nitrogen. **d.** Diffraction data is collected in beamline BL32XU .

3-2-3 Data collection and refinement

X-ray diffraction data were collected at a wavelength of 1.0 Å (100 K) on beamline BL32XU at SPring-8 with an EIGER X 9M (Dectris) detector. The ZOO and KAMO[15] (https://github.com/keitaroyam/yamtbx) systems were used for the automated crystal mounting, loop centering, data collection and data processing. From hundreds of crystals, small-wedge data (5° per crystal) were collected using 5×5 μm^2 beam. All datasets were indexed and integrated by XDS[16] and those indexed with similar latice parameters were scaled and merged with outlier rejections implemented in KAMO. For Zn^{2+}-ascorbate bound form, hierarchical clustering analysis based on unit cell parameters were performed using BLEND[17] prior to merging. The best cluster was selected based on the anomalous difference Fourier peak height at Zn^{2+}. Data collection statistics are summarized in Table 1. An initial model of Dcyt*b* was obtained by molecular replacement with Phaser[18]. *Arabidopsis thaliana* $Cytb_{561}$ (PDB code: 4O6Y) was used as the search model. The structure was refined with PHENIX[19], and model building was carried out with Coot[20]. ANODE[21] were used to calculate an anomalous difference Fourier map. The refinement statistics are summarized in Table 3-1. All structural figures were prepared with the PyMOL Molecular Graphics System (Version 2.0 Schrödinger, LLC).

3-2-4 Stopped-flow measurements

The rates of the reduction of wild type and variants of Dcyt*b* by ascorbate were determined by monitoring the absorbance change at 427 nm with a stopped-flow spectrophotometer (UNISOKU RSP-1000). For most experiments, concentrations of Dcyt*b* in the syringe of the stopped-flow instrument were 2 μM in the sample buffer containing HEPES (25 mM, pH 7.0, with NaCl (150 mM) and DDM (0.05% (w/v)). Protein solutions were degassed and placed under nitrogen prior to loading into the syringes. For the ligand solution, HEPES buffer (25 mM, pH 7.0, with NaCl (150 mM)) was degassed for 10 min and slowly purged with nitrogen for 30 min.

This buffer-ligand solution was mixed with a stock solution of 10% (w/v) of DDM (final concentration: 0.05% (w/v), and 20 mM sodium ascorbate (final concentrations: 2 μM - 5 mM). The temperature of the sample chamber was maintained at 20 °C with a thermal circulator. Five measurements of the time course of the reduction of oxidized Dcyt*b* with various concentration of ascorbate were measured and averaged. The data were fitted by a combination of four exponential functions using Igor Pro 6 software (Wavemetrics). The rate constants of the fastest phase k_1 (s^{-1}) were plotted against the ascorbate concentrations, and the dissociation constant K_s and rate constant k_{max} in the reaction of ascorbate-dependent heme reduction were obtained by equation (1).

$$k_1 = \frac{k_{max}[\text{Ascorbate}]}{K_s + [\text{Ascorbate}]} \quad \text{Equation (1)}$$

3-2-5 Resonance Raman spectroscopy

Resonance Raman spectra were recorded with a liquid nitrogen-cooled CCD detector (Roper Scientific, Spec 10:400B/LN) attached to a single polychromator (Jovin Yvon, SPEX750). The 441.6 nm line from a He-Cd laser (Kinmon Electric, model CD4805R) was adjusted to 5 mW at the sample point for excitation. Raman scattering was collected at right angles to the incident light and focused on the entrance slit (150 μm) of the polychromator. Spectra were obtained at ambient temperature with a quartz spinning cell (2,000 rpm) having a diameter of 8 mm. Raman shifts were calibrated with indene. The Dcyt*b* samples (final concentration 20 μM) with various concentrations of $ZnCl_2$ (0-10 mM) were prepared in Tris-HCl buffer (50 mM, pH 8.0, containing NaCl (150 mM) and DDM (0.025%)) and were introduced into the Raman cell sealed with a rubber septum. The samples were reduced by the addition of dithionite solution (final concentration 200 μM) under an N_2 atmosphere. Electronic absorption spectra were recorded before and after the Raman measurements to confirm that the samples were not damaged by laser irradiation.

Raman spectra were analysed with Igor software (WaveMetrics). After baseline correction, the spectra were normalized to the intensity of the ν_7 line at 675 cm^{-1}. Raman signals around 365-385 cm^{-1} were deconvoluted as two Gaussian functions. The dissociation constant (K_d) for Zn^{2+} binding to Dcyt*b* was calculated by fitting the titration data to equation (2), which assumes the presence of a single binding site for Zn^{2+}.

$$S_{obs} = S_0 + (S_{max} - S_0) \times \frac{[\mathrm{Dcyt}b] + [\mathrm{Zn}^{2+}] + K_d - \sqrt{([\mathrm{Dcyt}b] + [\mathrm{Zn}^{2+}] + K_d)^2 - 4[\mathrm{Dcyt}b][\mathrm{Zn}^{2+}]}}{2[\mathrm{Dcyt}b]}$$

Equation (2)

In this equation, S_{obs} denotes the estimated area of the Gaussian signal at 381 cm^{-1}, S_{max} and S_0 represent the area of the Gaussian peak at 381 cm^{-1} for Zn-free and Zn-bound samples, respectively, and [Dcyt*b*] and [Zn^{2+}] denote the total concentrations of Dcyt*b* and Zn^{2+} in the sample solution, respectively.

3-2-6 Ferric reductase activity assay

*Saccharomyces cerevisiae hem1*Δ*fre1*Δ*fre2*Δ YPH499 strain (*hem1*::KanMX *fre1*::LEU2 *fre2*::HIS3)[22] was used for the Fe^{3+} reductase activity assay. Because yeast gene *hem1* encodes ALA synthase that catalyzes synthesis of ALA, the first step of heme biosynthesis, all growth media were supplemented with 250 μM ALA to assure adequate heme synthesis for production of Dcyt*b*. Fe^{3+} reductase activity exhibited by this transformed yeast mutant was entirely attributable to expression of the enzyme from the high copy-number plasmid pYES-DEST52 (Thermo Fisher Scientific) carrying the yeast codon-optimized human *Dcytb* gene. Yeast transformation and selection were initially performed following growth on appropriate synthetic complete (SC) medium supplemented with raffinose (2% w/v) and ALA (250 μM). The resulting cells were suspended and grown in SC medium containing raffinose (2% w/v), ALA (250 μM), and galactose (0.4% w/v) for induction of Dcyt*b* expression or glucose (0.4% w/v) for suppression

of Dcyt*b* expression at 30 °C for 24 hours and subjected to Fe^{3+} activity assay[23]. Dcyt*b* expression was evaluated by Western blot analysis with the anti-human Dcyt*b* mouse monoclonal antibody (homemade, clone 11-2.1). Cells were washed with washing buffer (BSA (2% w/v), Tween 20 (0.1% w/v) in 2×PBS) and then washed twice with reaction buffer (glycerol (5% w/v) and sodium citrate buffer (50 mM, pH 6.5)). Cells suspended in reaction buffer were distributed into 96-well plates, and A_{600nm} was measured with a plate reader (SpectraMax 190, Molecular Devices). An equal volume of assay buffer (reaction buffer containing bathophenanthroline disulfonate (BPS) (2 mM) and $FeCl_3$ (2 mM)) was added to the cells (T = 0) and incubated in the dark at 30°C, 225 rpm until a red color developed. Absorbance values at 535 and 610 nm were determined, and Fe^{3+} reductase activity (nmol 10^6 $cells^{-1}$ $hour^{-1}$) was calculated with equation (3).

$$\frac{[(A_{535nm(sample)} - A_{610nm(sample)}) - (A_{535nm(blank)} - A_{610nm(blank)})] \times 45}{V_{cells} \times (A_{600nm(sample)} - A_{600nm(blank)}) \times T_{hour}} \quad \text{Equation (3)}$$

The resulting values of Fe^{3+} reductase activity were divided by the amount of Dcyt*b*, wild-type and variants, in each reaction mixture as estimated from the areas of the bands observed on Western blots with ImageJ software[24]. To examine the competitive binding assay between Fe^{3+} and Zn^{2+}, 0.00, 0.25, 0.50, 0.75, and 1.00 mM $ZnSO_4$ was added to the assay buffer containing 2 mM $FeCl_3$. To investigate the effects of dietary metal-chelators, the Fe^{3+} activity assay was performed in reaction buffer containing glycerol (5% w/v) with HEPES (50 mM, pH 6.8) or Tris (20 mM, pH8.0) and assay buffer containing 2 mM chelator (sodium citrate, malic acid or oxalic acid) and 2 mM $FeCl_3$.

The role of this C-terminal region in Fe^{3+} reductase activity by *in vivo* yeast functional assay. For that, *C*-terminal truncated (by 60 amino acid residues) codon optimized Dcyt*b*, with *C*-terminal hexa-His tag, cloned into pYES-DEST52 vector, was transformed into *Saccharomyces cerevisiae fre1*Δ*fre2*Δ mutant strain. The protein expression from the membrane crude was then evaluated by Western blot analysis with both anti-human Dcyt*b* mouse monoclonal antibody (homemade, clone 11-2.1) and anti-His tag antibody.

Table 3-1. Statistics of X-ray diffraction data collection and refinement

	Dcyt*b* (substrate-free)	Dcyt*b* (Zn^{2+} and Asc bound)
Data collection		
Beamline (SPring-8)	BL32XU	BL32XU
Space group	*C*2	*C*2
Wavelength (Å)	1.0	1.0
Cell dimensions		
a, b, c (Å),	64.45, 115.94, 48.43	65.19, 115.57, 48.60
α, β, γ (°)	90.00, 118.45, 90.00	90.00, 118.44, 90.00
Resolution (Å) [a]	50-2.6 (2.76 – 2.60)	50 – 2.8 (2.97 – 2.80)
Nr of merged crystals	866	600
Observed reflections	698,003	387,956
Unique reflections	9,644	7,824
Average $I/\sigma(I)$ [a]	10.0 (1.1)	8.5 (1.0)
Completeness (%) [a]	99.3 (99.3)	99.3 (99.7)
Redundancy [a]	72.4 (68.7)	49.6 (48.8)
$CC_{1/2}$ (%)	98.6 (68.8)	96.7 (48.1)
R_{pim} (%) [a,b]	11.8 (91.2)	22.5 (306.9)
Wilson *B*-factor ($Å^2$)	26.9	30.9
Refinement		
R_{work}/R_{free} (%) [c]	19.7/24.5	20.6/25.3
Average *B* value ($Å^2$)	33.2	42.0
R.m.s.d bond (Å)	0.008	0.009
R.m.s.d angles (°)	1.19	1.25
Ramachandran plot [d]		
Favored region (%)	96.0	94.6
Outlier regions (%)	0.5	0.5
PDB entry	5ZLE	5ZLG
SBGrid entry	573	574

[a] Values in parentheses are for the highest-resolution shell.

[b] $R_{pim} = \Sigma_{hkl}\{1/(n-1)\}^{1/2}\, \Sigma_i|I_i(hkl)-\langle I(hkl)\rangle| \,/\, \Sigma_{hkl}\Sigma_i I_i(hkl)$, where n is the multiplicity of reflection hkl, and $\langle I(hkl)\rangle$ is the average intensity of i observations.

[c] $R_{work} = \Sigma_{hkl}|F_{obs}(hkl) - F_{calc}(hkl)|/\Sigma_{hkl}F_{obs}(hkl)$, where F_{obs} and F_{calc} are the observed and calculated structure factors, respectively. R_{free} was calculated with 5% of the reflections.

3-3 Results

3-3-1 Purification and crystallization of Dcyt*b*

Recombinant human Dcyt*b* was expressed in *Escherichia coli* and purified by nickel-affinity and size exclusion chromatography. The purified protein was stable and mono-disperse. The purity of Dcyt*b* was evaluated from the RZ value (a Soret peak maximum / $A_{280\ nm}$) and absorption spectrum. Fractions with RZ value ranging from 2.0-2.7 were pooled together (Figure 3-3).

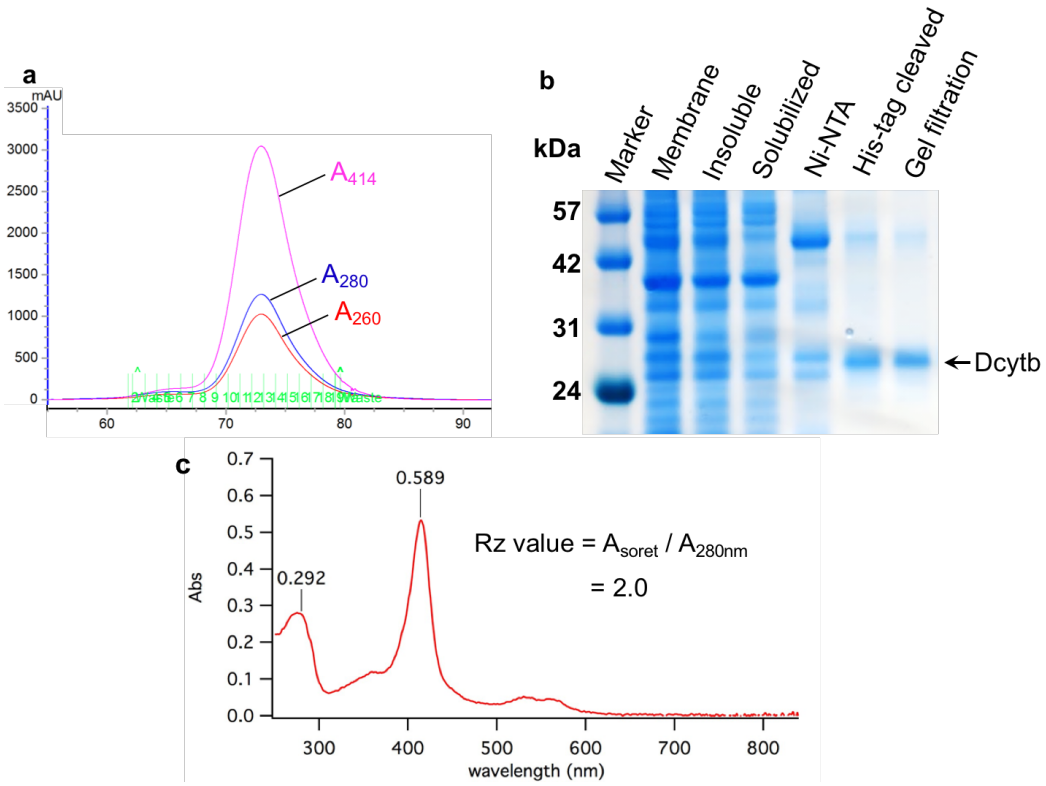

Figure 3-3. Protein purification profile. a. Purification chromatogram from gel filtration chromatography. The magenta, blue and red line represent absorbance at $A_{260\ nm}$, $A_{280\ nm}$ and $A_{414\ nm}$, respectively **b.** 10% SDS-PAGE of purified Dcyt*b*. **c.** UV visible absorption spectra of peak fractions from gel filtration chromatography.

The electronic absorption spectrum of these pooled fractions showed characteristic of the spectrum of bis-His coordinated hemoproteins with α- and β-bands observed at 531 and 561 nm, respectively, for the ferrous form (Figure 3-4). These spectra were essentially identical to those

previously reported for Dcyt*b* expressed in Sf9 cells[25] or *E. coli*. This recombinant Dcyt*b* was crystallized by LCP in the absence of substrate (ascorbate or metal ion). Crystals were initially observed in precipitant solution containing HEPES (pH 6.5) and jeffamine ED-2003 (20% (v/v)). The maximum growth of crystals ranged from ~4-8 μm (Figure 3-5).

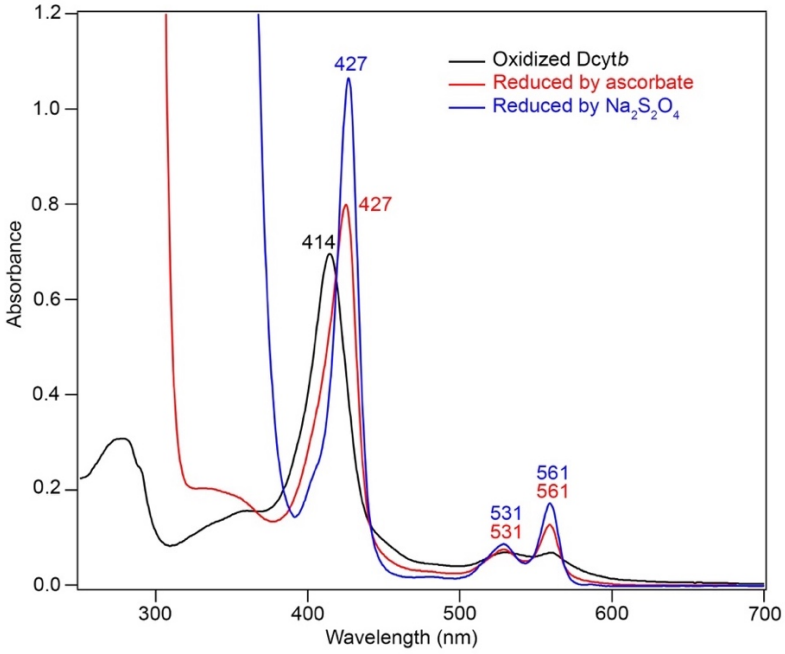

Figure 3-4. Electronic absorption spectra of oxidized and reduced Dcyt*b*. The spectrum of Dcyt*b* with ferriheme (black) is shown with the spectrum of Dcyt*b* with ferroheme reduced by ascorbate (red) and dithionite (blue). The spectrum was measured in MES-Na buffer (50 mM, pH 6.5) containing NaCl (150 mM) and DDM (0.025 %) at room temperature.

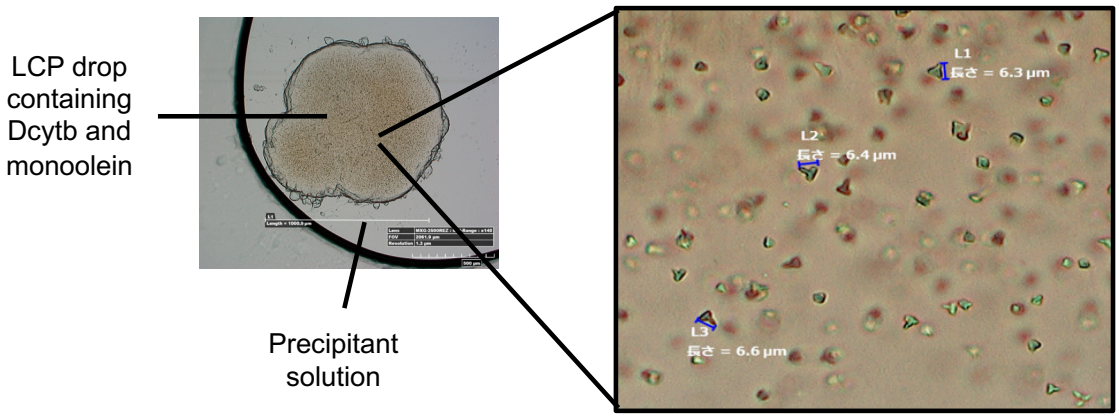

Figure 3-5. Crystals (~4-8 μm) of Dcyt*b* grown in LCP. The LCP crystallization drop consist of 50 nL protein sample in monoolein cubic phase, surrounded by 800 nL of precipitant solution containing HEPES (pH 6.5) and jeffamine ED-2003 (20% (v/v)).

3-3-2 Structural analysis of Dcyt*b*

Dcyt*b* crystal belongs to the *C*2 space group and allowed collection of X-ray diffraction data to a resolution of 2.6 Å. The structure derived from these data was determined by molecular replacement on the basis of the structure reported for *Arabidopsis thaliana* Cytochrome b_{561} (*At*Cytb_{561})[26], which exhibits 36% sequence identity with human Dcyt*b*. Dcyt*b* and *At*Cytb_{561} belong to the cytochrome b_{561} family, members of which have two heme cofactors per monomer and act as ascorbate-dependent oxidoreductases[4].

The overall structure of human Dcyt*b* is a homodimer in which each monomer possesses six transmembrane α-helices. The *N*- and *C*-termini are located on the cytoplasmic side of the protein (Figure 3-6a). The Dcyt*b* dimer exhibits crystallographic two-fold symmetry in which the monomers interact through hydrophobic interactions involving transmembrane helices α5 and α6 on the cytoplasmic side and helices α4, α5 and α6 on the apical side (Figure 3-7a & b). Although full-length Dcyt*b* (residues 1-286) was used for crystallization, the atomic model includes only residues 6–230 because the electron density map for the five *N*-terminal residues and the 56 *C*-terminal residues was disordered, most probably due to its conformational flexibility. The two heme *b* groups of each Dcyt*b* monomer are sandwiched between four central transmembrane helices (α2 to α5) at the apical (or luminal) and cytoplasmic ends of the structure and are referred to as such. As expected from the electronic absorption spectrum, each heme is hexacoordinate with H86 and H159 coordinating the iron of the cytoplasmic heme and H50 and H120 coordinating the apical heme iron (Figure 3-6b). All four of these ligands are highly conserved in the Cytb_{561} family. The A-propionate of the cytoplasmic heme forms a salt-bridge with the side chain of R70 from α2, and the corresponding D-propionate is exposed to the solvent (Figure 3-6c). The A-propionate of the apical heme forms a hydrogen-bond with the side chains of E180 from α5 and S118 from α4, and the D-propionate is hydrogen bonded with the side chain of N115 from α3 (Figure 3-6d). The closest edge-to-edge distance between the two heme groups within a monomer is 15.5 Å (Figure 3-6b).

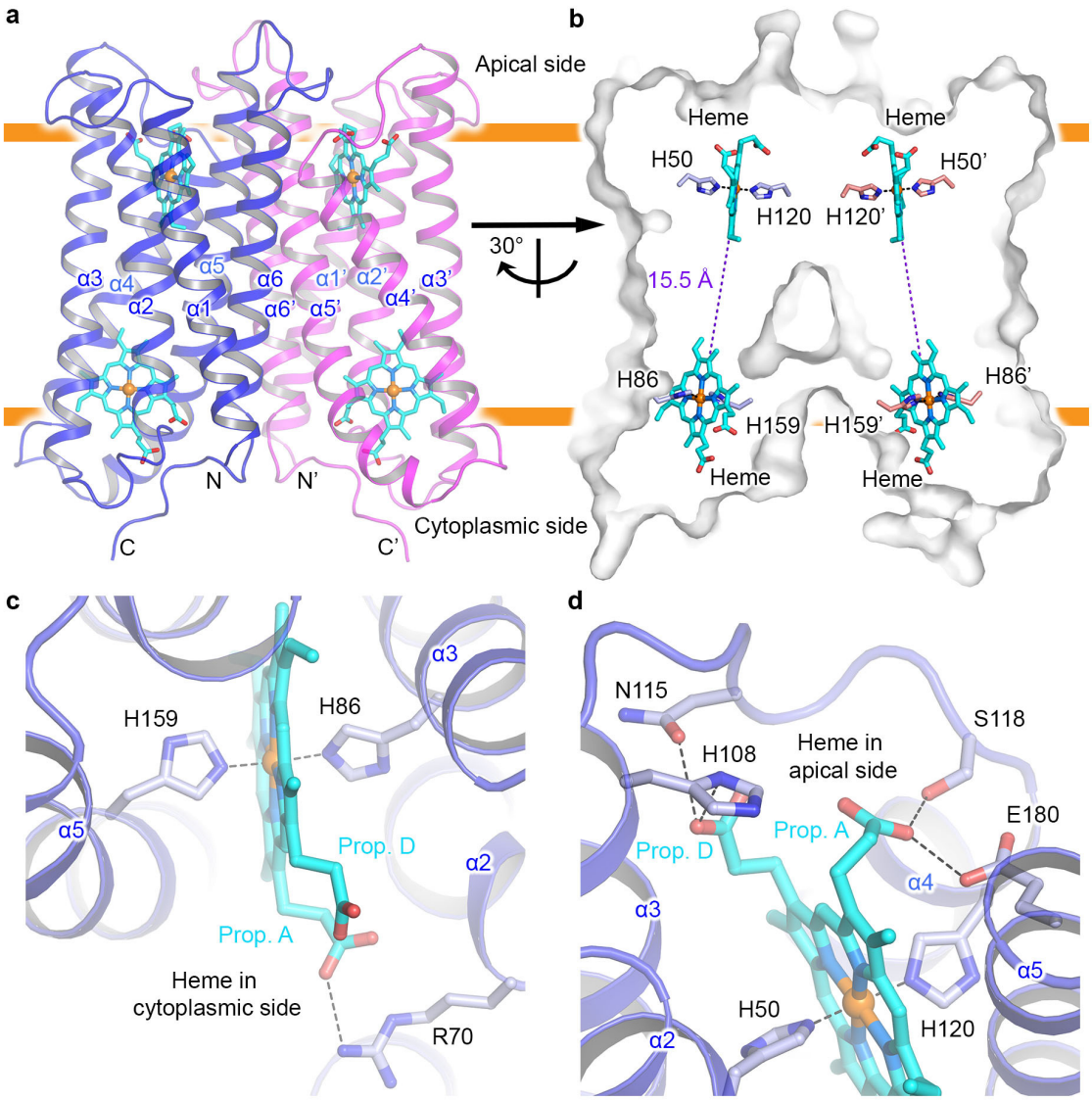

Figure 3-6. Overall structure of human Dcyt*b*. a. Ribbon representation of the Dcyt*b* homodimer. Each monomer consists of six α-helices (α1 - α6). Both N- and C- termini are located on the cytoplasmic side. Each monomer contains two heme b molecules, coordinated by four highly conserved His residues in a six-coordinate low spin form. **b.** The edge-to-edge distance between two heme molecules is 15.5 Å. **c.** The environment of the heme bound to the cytoplasmic side of Dcyt*b* is shown. **d.** The environment of the heme bound to the apical side of Dcyt*b* is shown.

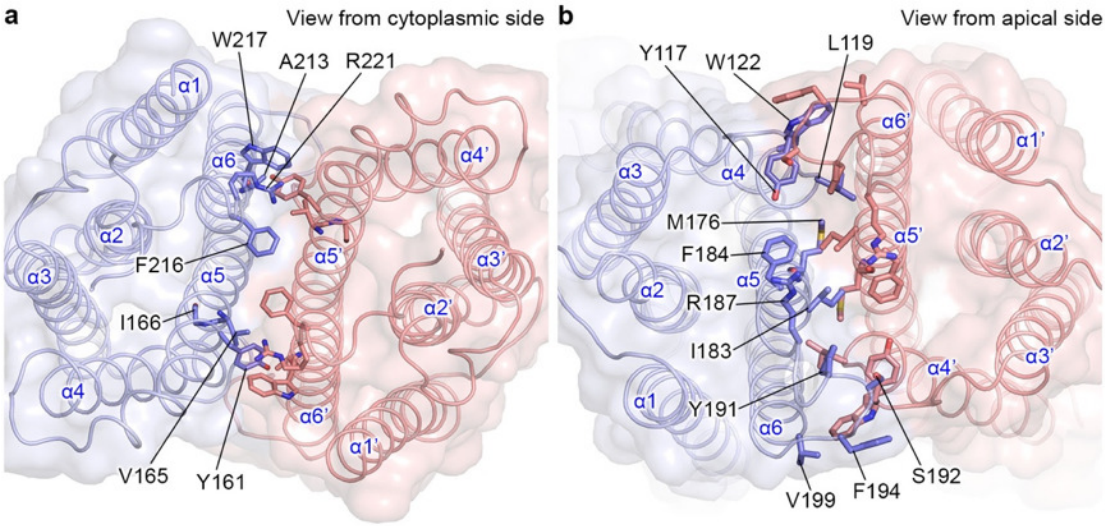

Figure 3-7. Homodimeric structure of Dcyt*b*. Residues from each monomer (shown in light blue and salmon) associate with each other through hydrophobic interactions. **a.** View from the cytoplasmic side. Hydrophobic interactions involve residues from α-helices 5 and 6 of each monomer. **b.** View from the apical side. Hydrophobic interactions involve residues from α-helices 4, 5 and 6 of each monomer.

To characterize the structural basis for ascorbate and metal ion binding to Dcyt*b*, we co-crystallized Dcyt*b* in the presence and absence of ascorbate with and without metal ions (Fe^{3+}, Cu^{2+} and Zn^{2+}) or other compounds such as ferric ammonium citrate and hydroxypyridone. Only soaking crystals with Zn^{2+} and ascorbate produced crystals that diffracted X-rays well. Although Fe^{3+} and Cu^{2+} are substrates for Dcyt*b*, these metal ions are spontaneously reduced by ascorbate, and reduction affects the affinity for the protein or damages the crystal. Zn^{2+} is not redox active and is generally known to bind proteins in a manner similar to that of Fe^{3+} [27-29]. Consequently, Zn^{2+} was used as an alternative to Fe^{3+} in soaking experiments with ascorbate.

The overall structure of Dcyt*b* with Zn^{2+} and ascorbate bound was determined at 2.8 Å resolution. This structure exhibited no significant conformational change from the structure of Dcyt*b* determined in the absence of Zn^{2+} and ascorbate (rmsd 0.4 Å for all Cα atoms). Close-up view at the cytoplasmic and apical side also showed no huge change between apo and holo form, except for the disordered electron density of F47 (Figure 3-8).

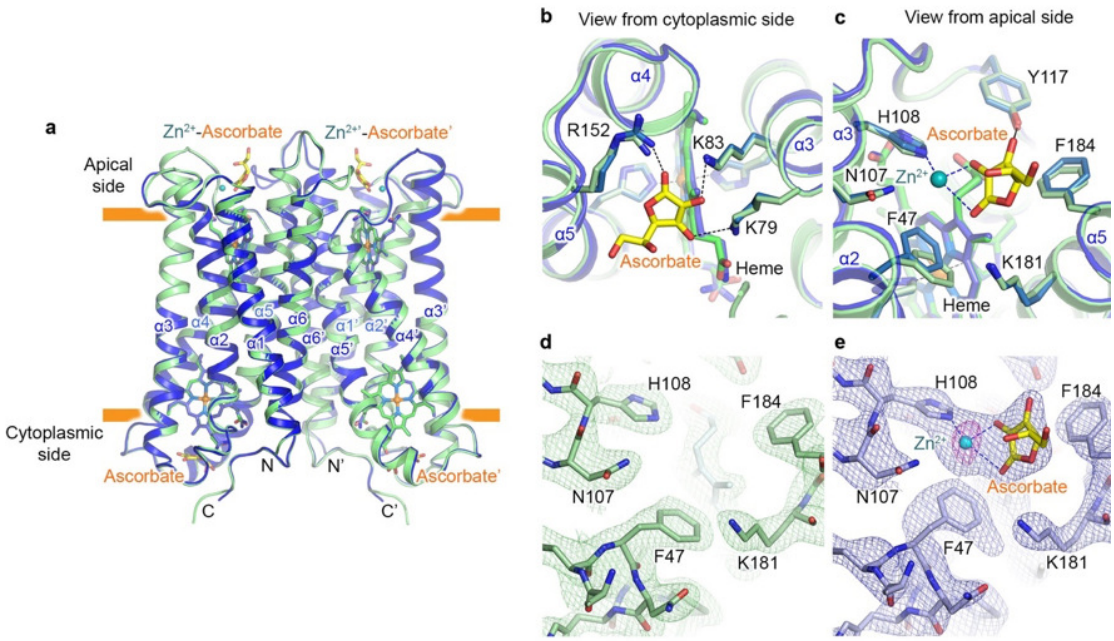

Figure 3-8. The superposition of apo- and holo- Dcyt*b*. a. The six α-helices of the substrate-free (green) were superimposed on those of the substrate-bound structure (blue) with an r.m.s.d. of 0.4 Å for all Cα atoms. **b.** Close-up view of the superposition from the cytoplasmic side. Residues that interact with ascorbate are shown as sticks. **c.** Close-up view of the superposition from apical side. Residues that coordinate Zn^{2+}-ascorbate are shown as sticks. Of the amino acid residues in this vicinity, only F47 exhibits any change in orientation upon Zn^{2+}-ascorbate binding. **d.** Electron density map of residues around apical side of apo-Dcyt*b*, contoured at 1.5σ. **e.** Electron density map of residues around apical side of holo-Dcyt*b*, contoured at 1.5σ. Density of F47 changed upon Zn^{2+}-ascorbate binding.

Clear electron density for substrate binding was observed at both the cytoplasmic and apical sides of the protein. The electron density from one ascorbate molecule was observed on the cytoplasmic surface of Dcyt*b* in proximity to the heme located near the cytoplasmic surface (Figure 3-9a). Note that in these results, ascorbate cannot be distinguished from the oxidized form, monodehydroascorbate, so for simplicity we refer only to ascorbate in this report. Consistent with the properties of ascorbate, the ascorbate-binding pocket on the cytoplasmic side contains three positively charged residues: the 1-ketone group of ascorbate is hydrogen bonded with R152 from α5, and the hydroxyl groups at positions-2 and -3 are hydrogen bonded with K83 and K79 from α3, respectively (Figure 3-9a & b). These three residues are highly conserved in the Cytb_{561} family. In addition, the 5-methyl group of the cytoplasmic heme group is within van der Waals distance of the lactone ring of ascorbate.

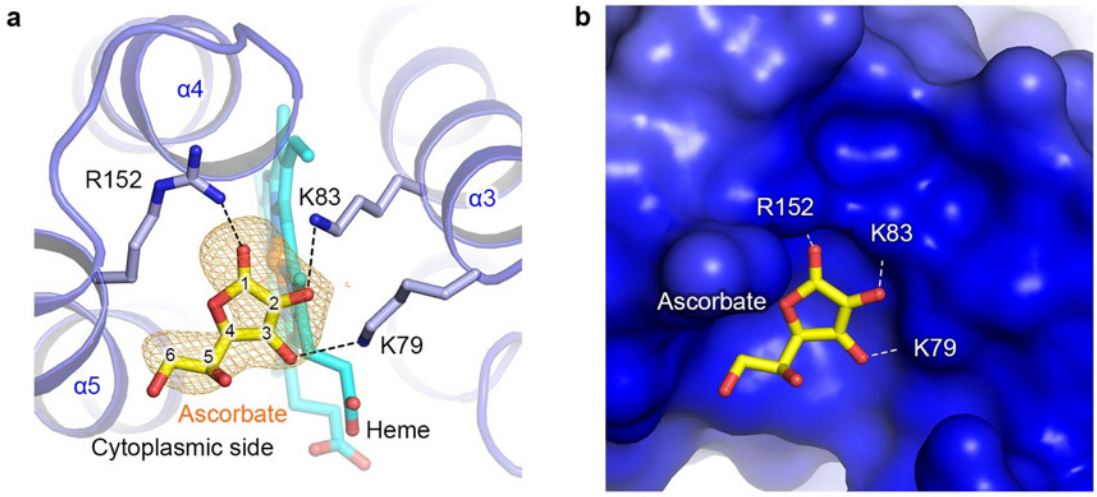

Figure 3-9. Substrate binding on the cytoplasmic side of Dcyt*b*. a. Ascorbate is bound on the cytoplasmic surface of Dcyt*b* by interacting with three positively charged residues. The omit map for ascorbate is contoured at 2.5σ (orange mesh). **b.** The positively charged cavity for ascorbate-binding on the cytoplasmic surface is shown.

The importance of these three residues in the ascorbate binding site was investigated by stopped-flow kinetics studies of ascorbate reduction of the K79S, K83S and R152E variants (Figure 3-10 and Table 3-2). The rate of heme reduction was decreased by these substitutions. Similar results were reported following substitution of the corresponding residues in *At*Cytb$_{561}$[26]. These kinetic results provide evidence that these three residues contribute to efficient electron transfer from the cytoplasmic ascorbate to the adjacent heme group of Dcyt*b*. Most probably, the mutation of one of these three residues would cause slight distortion in the ascorbate binding, resulting in slower rate of electron transfer from cytoplasmic ascorbate to heme center. The protein-ascorbate interaction observed in cytoplasmic surface of Dcyt*b* shows some similarity to that in ascorbate peroxidase (APX)[30] in which two positively charged residues (K30 and R172) interact with ascorbate. However, these two sites differ in a way that a heme propionate and main chain carbonyl group also interact directly with ascorbate in APX and that the location and orientation of ascorbate with respect to the heme are different.

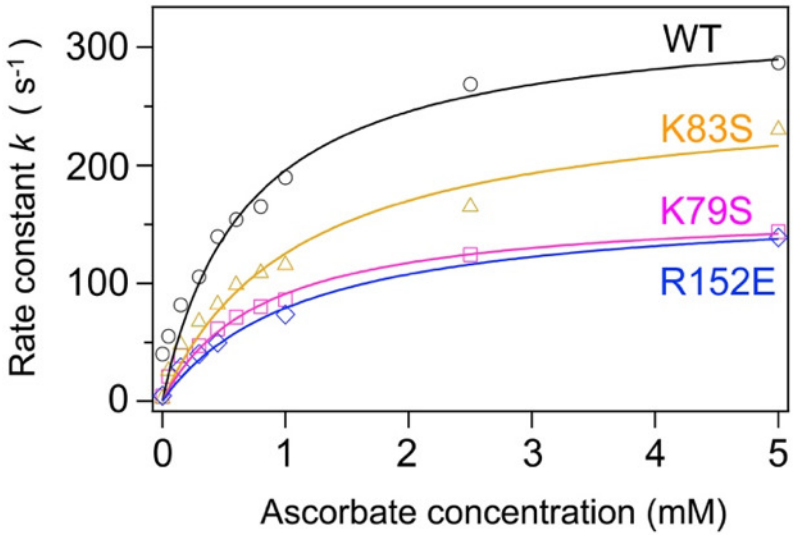

Figure 3-10. Dependence of the initial phase of heme reduction of wild-type and variant forms of Dcyt*b* on [Ascorbate]. In comparison to the wild-type enzyme, the rates of K79S and R152E reduction are nearly halved while the rate of K83S reduction is reduced by ~20%.

Table 3-2. Comparison of dissociation constant and rate constant in the reaction of ascorbate-dependent heme reduction.

	K_s (mM)	k_{max} (s^{-1})
Wild type	0.68±0.07	330±10
K79S	0.81±0.05	165±4
K83S	1.1±0.2	270±20
R152E	1.1±0.2	170±10

The metal ion binding site was identified by an anomalous difference Fourier map (Figure 11). Specifically, a strong electron density observed on the apical side of Dcyt*b* near the apical heme and H108 was assigned to Zn^{2+}. This Zn^{2+} is coordinated to the $N\varepsilon_2$ atom of H108 at a distance of 2.0 Å. In addition to the density for Zn^{2+}, an additional density was observed very close to the Zn^{2+}. This extra density appears as a flat shape in the F_o-F_c map that occurs parallel to F184 and that we attribute to a bound ascorbate (Figure 3-11). This arrangement means that Zn^{2+} binding to Dcyt*b* involves coordination to ascorbate. The distances of Zn^{2+} to the O-2 and

O-1 atoms of ascorbate are 2.2 Å and 2.8 Å, respectively, and the Nε_2(H108)-Zn^{2+}-O-2(ascorbate) angle is 89º. N107 is not coordinated to Zn^{2+} but is nearby (3.4 Å). The only other interaction of ascorbate with the protein occurs through van der Waals contact with F184, which resides 3.5-4.0 Å from the lactone ring of ascorbate. The weak electron density of the ascorbate dihydroxyethyl group (C5 and C6 position) probably results from lack of any interaction with the protein. Although the side chains of Y117, K181 and R187 contribute to the formation of the large pocket on the apical surface, these residues do not interact directly with ascorbate through hydrogen-bonding or salt bridge formation (Figure 3-11a & b).

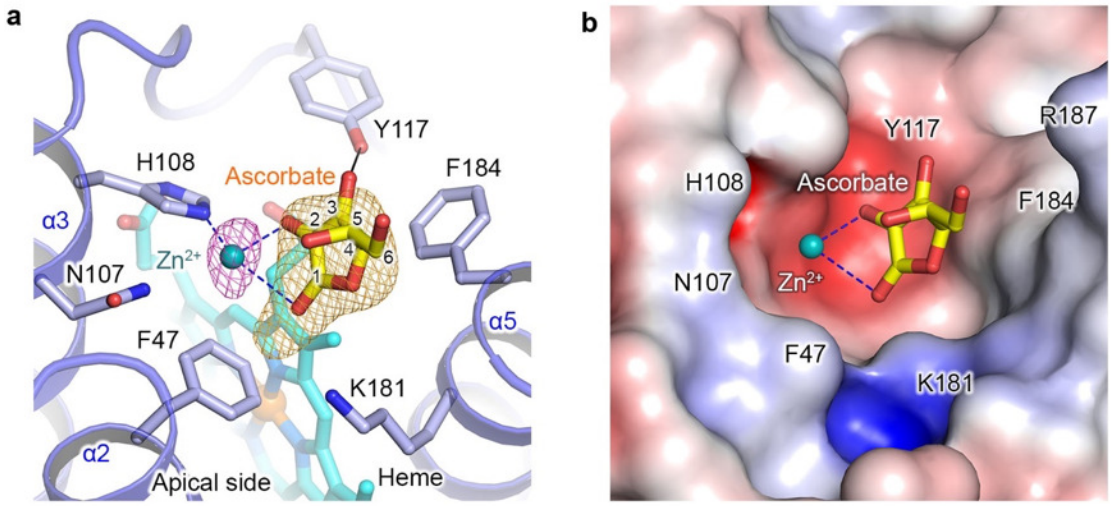

Figure 3-11. Substrate binding on the apical side of Dcyt*b*. a. The Zn^{2+} binding to H108 and two hydroxyl groups of ascorbate on the apical surface of Dcyt*b* is shown. The anomalous difference Fourier map (magenta mesh) calculated from X-ray data collected with 1.0 Å wavelength is contoured at 3.5σ. The omit map for ascorbate (orange mesh) bound to the apical side is contoured at 4.0σ. **b.** The Zn^{2+}-ascorbate-binding cavity on the apical surface is shown.

3-3-3 Analysis of metal binding by resonance Raman spectroscopy

To characterize Zn^{2+}-binding to H108 of Dcyt*b* further, we studied wild-type Dcyt*b* and the H108Q variant in the presence and absence of ascorbate and Zn^{2+} by resonance Raman spectroscopy (Figure 3-12).

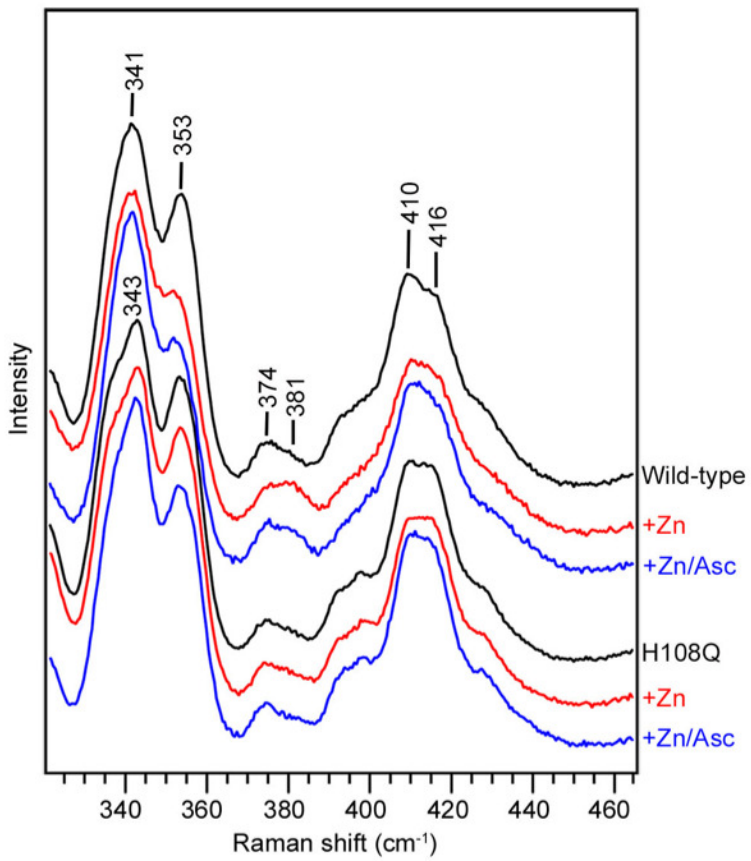

Figure 3-12. Resonance Raman analysis of Zn^{2+} binding to reduced Dcyt*b*. The low frequency region of the resonance Raman spectrum of Dcyt*b* in the absence and presence of $ZnCl_2$ (5 mM) or $ZnCl_2$ (5 mM) and ascorbate (20 mM) are shown for the wild-type and H108Q variant proteins.

As the heme irons of Dcyt*b* are partially reduced upon laser irradiation, we focused on Zn^{2+} binding to the reduced form, but not the oxidized form, of Dcyt*b*. We collected spectra of Dcyt*b* in the presence of $Na_2S_2O_4$ to assure that the heme irons were fully reduced. Upon addition of ascorbate to either protein, no spectroscopic changes were observed in either the high or low frequency regions, indicating that ascorbate binding to Dcyt*b* induces no significant structural changes around the hemes. On the other hand, addition of Zn^{2+} to wild-type Dcyt*b* in the presence or absence of ascorbate induced the appearance of a small band at 381 cm^{-1} in the low frequency region. Since the 381 cm^{-1} band was assigned as a bending vibration of the heme propionate groups[31], the Zn^{2+} binding could induce the change of the environment of the heme propionate group. This change in spectrum was not observed following addition of Zn^{2+} or a mixture of Zn^{2+} and ascorbate to the H108Q variant. H108 is located adjacent to a propionate group of the apical

heme, so the appearance of the 381 cm^{-1} band in the presence of Zn^{2+} is consistent with participation of H108 in the binding of this metal ion as indicated by the crystallographic structure. By monitoring the increase in intensity of the 381 cm^{-1} band while titrating Dcyt*b* with Zn^{2+}, the dissociation constant for Zn^{2+} binding was estimated to be ~0.5 mM (Figure 3-13 & 3-14).

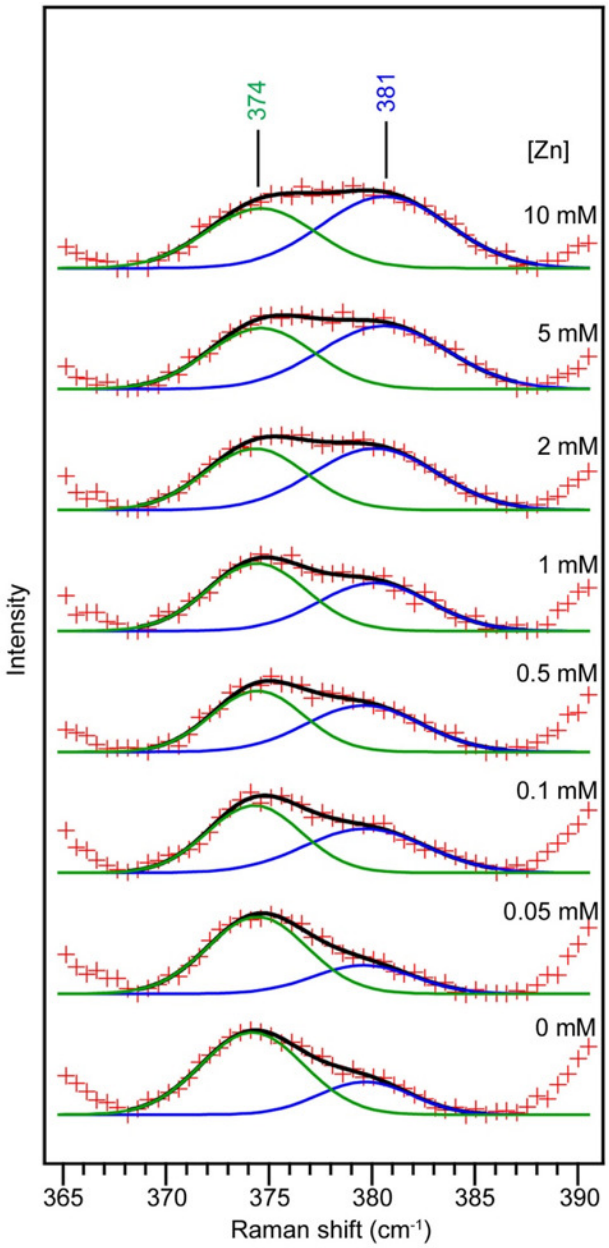

Figure 3-13. Titration of Dcyt*b* with Zn^{2+} as monitored by resonance Raman spectroscopy. The resonance Raman spectra of reduced Dcyt*b* in the presence of various concentrations of Zn^{2+} (red symbols) were obtained with 441.6 nm excitation. The Raman signals around 365~385 cm^{-1} were deconvoluted as two Gaussian functions. Black traces represent the fit of these functions to the data. The Gaussian components at 374 cm^{-1} (green) and 381 cm^{-1} (blue) are shown.

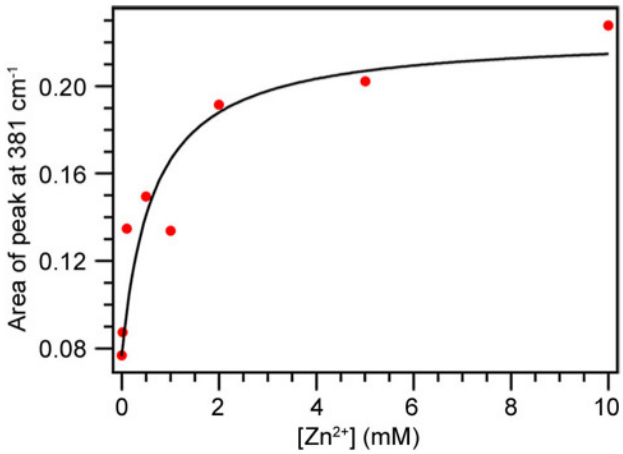

Figure 3-14. The titration of reduced wild-type Dcyt*b* with Zn^{2+} as monitored by resonance Raman spectroscopy at 381 cm^{-1}. The peak areas at 381 cm^{-1} are plotted as red circles as a function of [Zn^{2+}]. The black curve represents a fit of the data to equation 2 to provide an estimated K_d of 0.5 ± 0.1 mM.

We also examined the Fe^{3+} and Cu^{2+} titration of fully reduced Dcyt*b* in the presence of $Na_2S_2O_4$ but did not observe any change in the low frequency region of the resonance Raman spectrum. As observed during crystallization experiments, Fe^{3+} and Cu^{2+} can be reduced readily to Fe^{2+} and Cu^{1+}, neither of which binds to Dcyt*b* as observed by resonance Raman spectroscopy. This observation is consistent with the physiological expectation that both Fe^{2+} and Cu^{1+} should dissociate from Dcyt*b* for subsequent transport by DMT-1.

3-3-4 Analysis of electron transfer pathway in Dcyt*b*

The possible pathways for electron transfer from the cytoplasmic ascorbate to iron bound at the apical surface were explored with the *Pathways* plugin for VMD[32,33]. These calculations suggest three possible electron transfer pathways as shown in Figure 3-15: First, [cytoplasmic heme]→Y131→ F58 → [apical heme] → Fe^{3+} (or Cu^{2+}). This pathway includes three through-space transfers between the two hemes that have distances of 3.6~4.9 Å; Second, a pathway through a series of covalent and H-bonds along the helix α2 (orange dashed line); and Third, a pathway along the helix α4 (blue dashed line). These results are compared with those obtained from identical calculations for *At*Cytb_{561} in Figure 3-15. Despite the differences in structure

exhibited by these two proteins in the region between the two heme groups of each monomer, these calculations indicate that the pathways for electron transfer between two heme groups of each of these two proteins are remarkably similar.

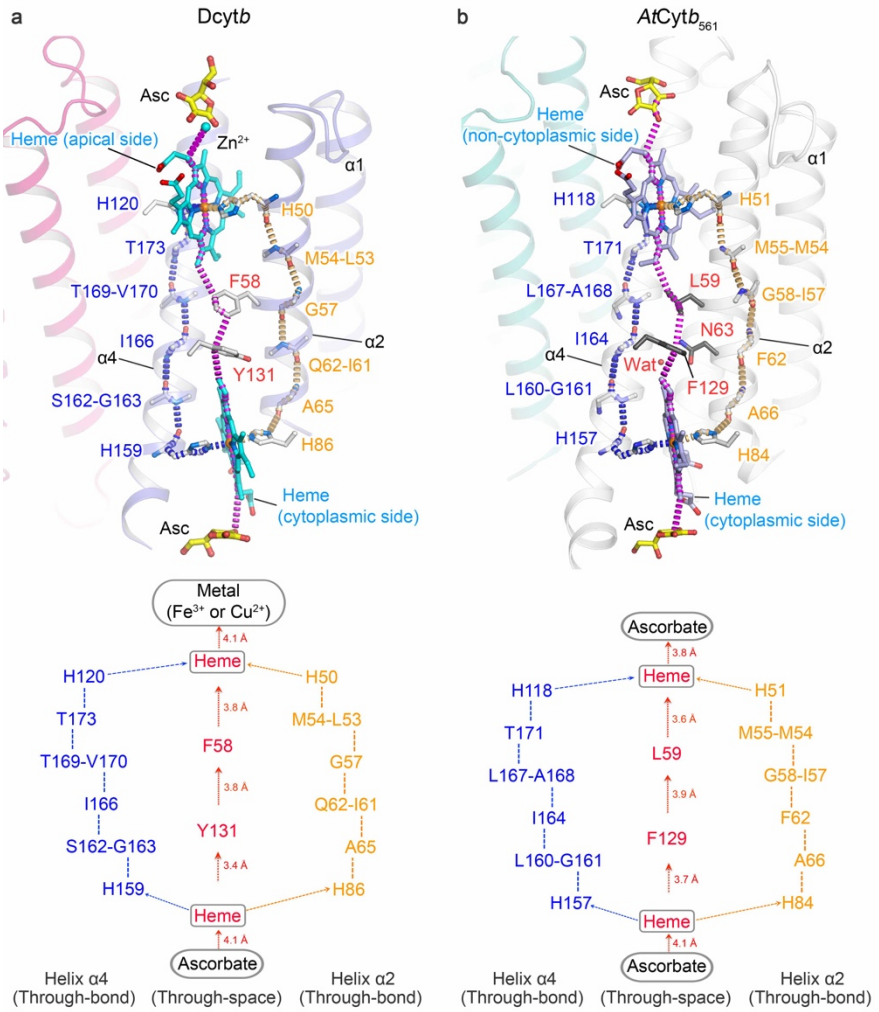

Figure 3-15. Proposed electron transfer routes of Dcyt*b* and *At*Cyt*b*$_{561}$. a. In Dcyt*b*, three possible routes can be proposed based on the current structure: First, through-space electron transfer (magenta dashed line) mediated by two aromatic residues (Y131 and F58), which are aligned within the distance of 4 Å. The F58 is substituted with Leu, Tyr or Met in most of other members of Cyt*b*$_{561}$ family, whereas Y131 is conserved or substituted with Phe in other members. Second, through-bond electron transfer (orange dashed line) mediated by series of amino acid residues along α-helix 2. Third, through-bond electron transfer (blue dashed line) mediated by series of amino acid residues along α-helix 4. **b.** In *At*Cyt*b*$_{561}$, a F129 and L59 mediated route (magenta dashed line), a route involving covalent and H-bonds along α-helix 2 (orange dashed line), and a route along α-helix 4 (blue dashed line) were suggested. A water mediated route (through space) has also been proposed for *At*Cyt*b*$_{561}$ by Lu et al.[20], although we could not reproduce it. The binding of water to N63 of *At*Cyt*b*$_{561}$ family because N63 is diverse. Indeed, this position corresponds to Q62 in Dcyt*b*, a substitution that results in no space for water.

3-3-5 Ferric reductase activity of Dcyt*b*

As shown above (Figure 3-11), H108, Y117, F184 and N107 contribute to the environment in the region of metal ion and ascorbate binding. To evaluate the functional roles of these residues, site-directed mutants of human Dcyt*b* were expressed in a yeast strain (*Saccharomyces cerevisiae fre1*Δ*fre2*Δ) that lacks the endogenous plasma membrane Fe^{3+} reductases, Fre1 and Fre2. Expression of wild-type human Dcyt*b* on the plasma membrane of this yeast mutant rescues the growth of this yeast by providing Fe^{3+} reduction required for nutritional iron absorption, that is normally provided by Fre1 and Fre2. In this system, electrons for Fe^{3+} reduction are supplied by cytoplasmic ascorbate produced by yeast ascorbate biosynthesis[34].

With this growth assay, we first examined the effect of Zn^{2+} binding on the Fe^{3+} reductase activity of wild-type and variant forms of Dcyt*b* (pH 6.5, sodium citrate buffer (50 mM), 5% w/v glycerol, conditions similar to those in the duodenum[35]). As [Zn^{2+}] was increased to 1.0 mM, ferric reductase activity of wild-type Dcyt*b* decreased by about 43% (Figure 3-16a), consistent with Zn^{2+} binding to the enzyme competitively with Fe^{3+}.

The functional roles of specific residues were studied next by evaluating the activities of several Dcyt*b* variants (Figure 3-16b). The H108A and H108Q variants exhibited the lowest Fe^{3+} reductase activities (20 and 25%, respectively) of those studied. These results are consistent with the proposal that H108 is a ligand for the binding of Fe^{3+} as well as Zn^{2+}. Although N107 is not a Zn^{2+} ligand, the amide nitrogen is just 3.7 Å from the bound metal ion, so presumably the site for binding of the Fe^{3+}-ascorbate complex in the structure of the N107F variant is perturbed sufficiently to accounts for the 35% activity resulting from this substitution. Interestingly, even though Y117 is ~6.6 Å from the bound Zn^{2+}, the Y117A and Y117S variants exhibited ~35% and 40% of the wild-type activity. Considering the relative proximity of Y117 to the adjacent ascorbate, it seems likely that the decreased activities of these variants results from perturbation of ascorbate binding, which would, in turn, affect binding of Fe^{3+}. A similar mechanism presumably accounts for the decreased activity exhibited by the F184A variant (~35% of wild-

type activity). Finally, the proposal that F58 and Y131 participate in the electron transfer pathway between the cytoplasmic and apical heme groups is consistent with the observation that the activities of the F58L and Y131L variants were less than 50% of wild-type Dcyt*b*.

Ferric iron is presented to Dcyt*b* in the duodenum in a variety of chelated forms because many potential soluble ligands for iron occur in this environment and in nutritional sources of iron. The relatively accessible binding sites for iron and ascorbate on the apical surface of Dcyt*b* appear to be compatible with this multiplicity of substrate forms (Figure 3-10), but the influence of likely iron ligands on Dcyt*b* activity is unknown. To investigate this issue, the effect of soluble chelators on the Fe^{3+} reductase activity of Dcyt*b* was evaluated by the individual supplementation of the yeast assay mixture with a variety of putative dietary chelating agents (Figure 3-16c). Citrate, which was used as a buffer in the kinetics experiments above, is a known dietary chelator that supports iron uptake from the gut[36]. As an excess of citrate may reasonably be expected to occupy the relatively accessible binding site for Fe^{3+} and ascorbate, the effect of soluble chelators on Fe^{3+} reduction was evaluated in non-chelating buffers. In addition, because the pH of digesting nutrients changes from acidic to basic with passage from the stomach to the duodenum[35], we studied Fe^{3+} reduction by Dcyt*b* under acidic (MES, pH 6.5) and basic (TrisHCl, pH 8.0) conditions (Figure 3-16c). These studies revealed that at acidic pH, the effect of added ligands on reductase activity was oxalate > citrate > no chelator > glucose~fructose > malate while at basic pH, this order was changed to citrate~oxalate > malate > no chelator~glucose~fructose. Notably, the ability of citrate, malate, and oxalate to accelerate Fe^{3+} reduction by Dcyt*b* is far greater at alkaline pH than at acidic pH.

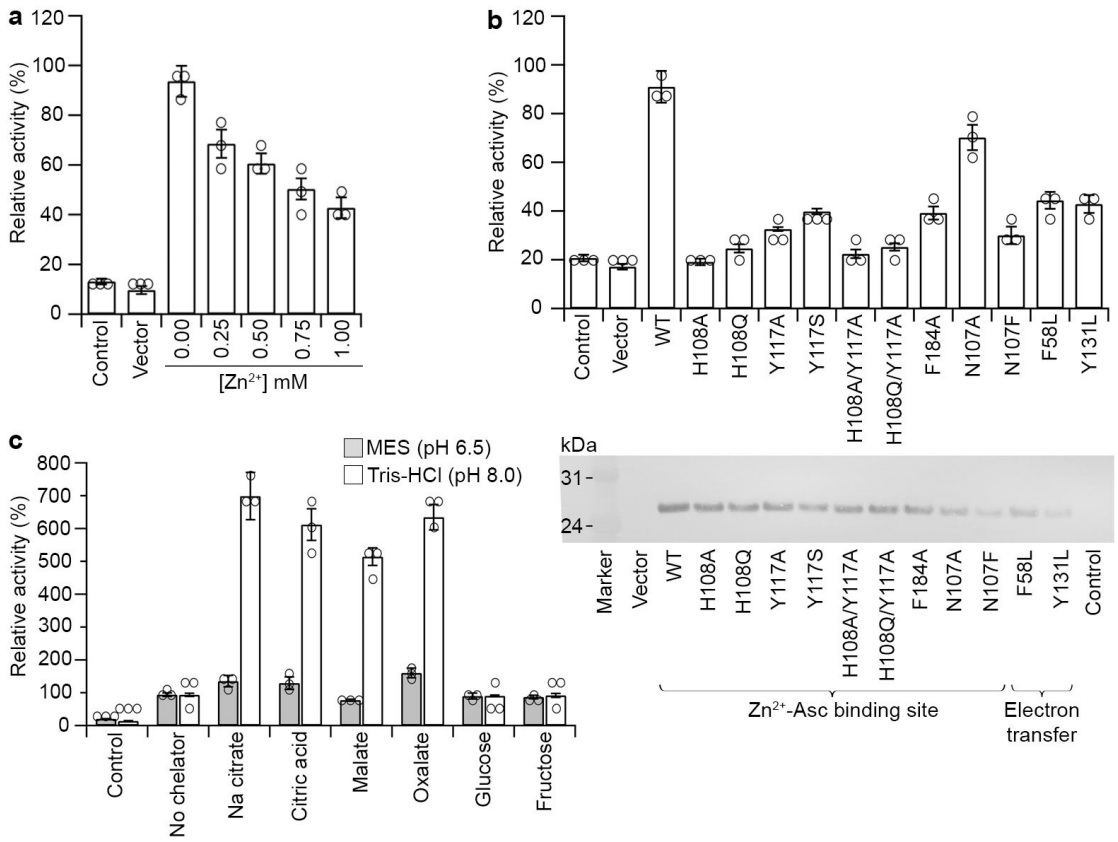

Figure 3-16. Ferric reductase activity of Dcyt*b*. The values indicated are means ± S.D. of data from duplicate sets of samples analyzed in triplicate. The "Control" means that the Dcyt*b* expression was suppressed in the transformant of wild-type *dcytb* cDNA-inserted vector, and the "Vector" shows that the expression vector (no insertion of *dcytb* gene) was transformed and performed same culture with wild-type and other variants. Dot-plot (empty circle) shows the data distribution. **a.** Competitive binding between Fe^{3+} and Zn^{2+} in wild-type Dcyt*b*. The value of 0 mM (~220 nmol 10^6 $cells^{-1}$ $hour^{-1}$) was set to 100% and the relative activity was obtained for increasing Zn^{2+} concentration. **b.** Fe^{3+} reductase activities of the structure-guided mutants of Dcyt*b*. Western blot of whole cell lysate of Dcyt*b*-expressed yeasts (1.0 μg protein per lane) shown in the bottom. **c.** Effect of dietary metal-chelators on Fe^{3+} reductase activity in wild-type Dcyt*b*. The effect of chelators was tested in MES buffer (pH 6.5) and Tris-HCl buffer (pH 8.0). The activity without chelator for MES buffer (~195 nmol 10^6 $cells^{-1}$ $hour^{-1}$) and Tris-HCl buffer (~65 nmol 10^6 $cells^{-1}$ $hour^{-1}$) was set to 100%, and the relative activity with chelators was calculated for respective buffers.

3-4 Discussion

Human ferric reductase Dcyt*b* is an essential enzyme for enteric iron absorption and a member of Cytb_{561} protein family, which utilizes cytoplasmic Asc as electron donor for the reduction of a substrate in non-cytoplasmic side, in which two heme *b* molecules mediate intra-molecular electron-transfer reaction across the membrane. The substrate is either Fe^{3+} or monodehydroascorbate (MDA), depending on their subcellular localization. The principal substrate of the enteric enzyme Dcyt*b* is Fe^{3+} while that of the adrenal and plant enzymes is monodehydroascorbate. The adrenal enzyme resides in chromaffin granules (CGcyt*b*) and reduces intra-vesicular monodehydroascorbate for regeneration of ascorbate that is used in the biosynthesis of the neurotransmitter norepinephrine[37]. Nevertheless, the CGcyt*b* and the lysosomal enzyme (Lcyt*b*) have also been shown to be capable of catalyzing Fe^{3+} reduction by ascorbate[38]. The role of Cytb_{561} in the Asc regeneration is well described in a most recently reported crystal structure of plant Cytb_{561} from *Arabidopsis thaliana* (*At*Cytb_{561})[26]. This report was the first Cytb_{561} family member that has been structurally characterized. This structure provided potential binding sites for Asc and MDA, which may potentiate its enzymatic activity. The structural comparison between human Dcyt*b* and plant *At*Cytb_{561} could provide valuable insights into the mechanism of the Fe^{3+} reduction by Dcyt*b*.

3-4-1 Sequence alignment of Dcyt*b*

The sequence of the human Dcyt*b* core structure (residues 6-230) shares 36% identity and 52% similarity with that of the plant enzyme *At*Cytb_{561} (residues 9 to 220). Comparison of these two structures reveals that the six α helices (163 Cα atom pairs) are superimposable with a rmsd of 0.6 Å despite the conformational differences observed in the loop regions that connect the α helices. Moreover, the relative orientations of monomers within these two dimers differ by only 5º. The overall structure is well conserved among all Cytb_{561} family members. One significant difference in the sequence of Dcyt*b* relative to other members of this family is the presence of an

additional 56 residue C-terminal region that is absent from the *At*Cyt*b*$_{561}$ MDA reductase. This region is located on the cytoplasmic side of the protein and is disordered in the structure of Dcyt*b* reported here.

Three human proteins belonging to the Cyt*b*$_{561}$ family, Dcyt*b* (duodenal brush border membrane), Lcyt*b* (late endosomal-lysosomal membrane), and CGcyt*b* (chromaffin granule), differ in the length of this C-terminal region (Figure 3-17).

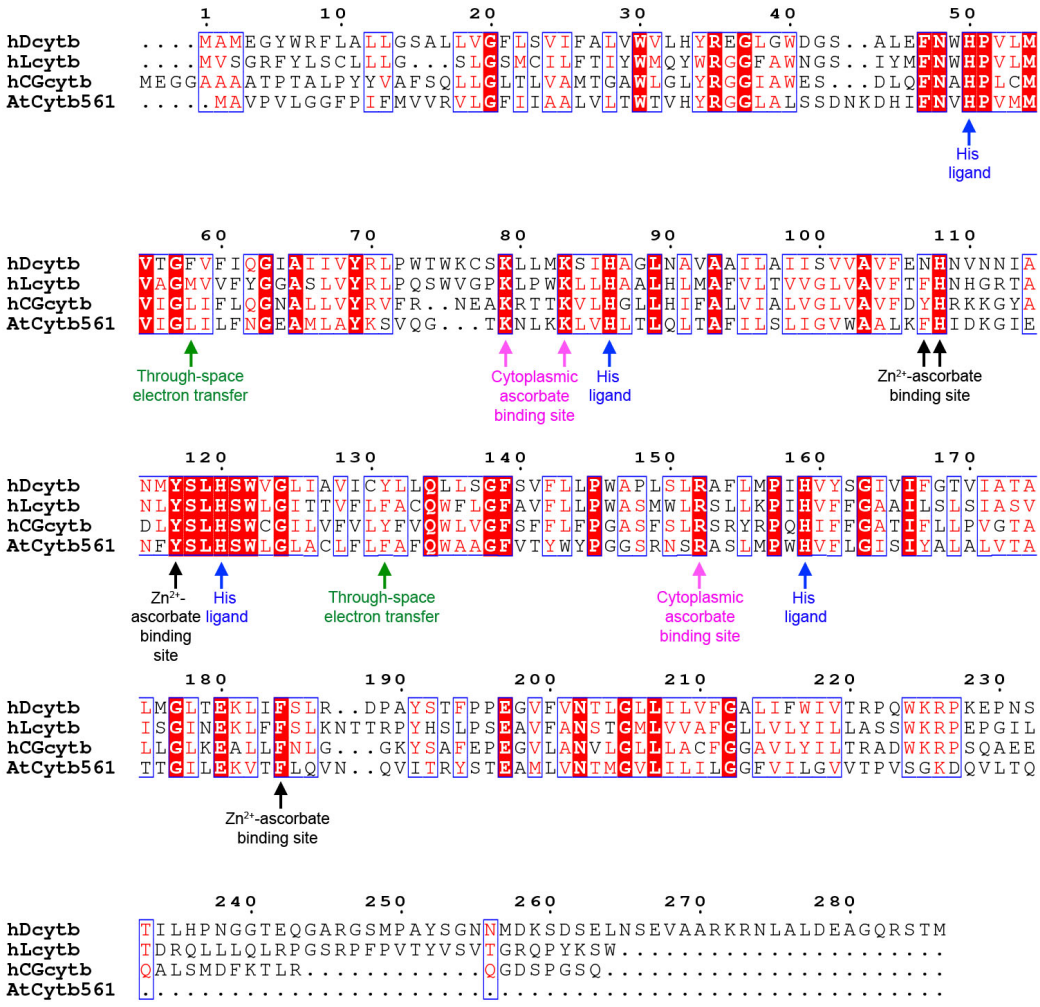

Figure 3-17. Sequence alignment of Dcyt*b* with *At*Cyt*b*$_{561}$ and other human members of Cyt*b*$_{561}$ family. The four sequences shown here are duodenal Cyt*b* (Dcyt*b*), late-endosomal Cyt*b* (Lcyt*b*), chromaffin granule Cyt*b* (CGcyt*b*) from *Homo sapiens*, and Cyt*b*$_{561}$ from *Arabidopsis thaliana* (*At*Cyt*b*$_{561}$). Residues conserved in all four sequences are highlighted in red. Dcyt*b* has a C-terminal sequence that is longer than all other members of this family.

This solitary difference might be the key to the difference in function and localization of various Cytb_{561}. Considering that Dcyt*b* and Lcyt*b* act as Fe^{3+} reductases while CGcyt*b* acts as an MDA reductase, this C-terminal region may be related to the subcellular locations of the enzymes or to their physiological functions. The extra-long C-terminal peptide is conserved only in Dcyt*b* of human and mouse[39], both of which are expressed in duodenal brush border membrane and function as ferric reductase. Indeed, a study reported the role of *C*-terminal sequence in mediating the localization of human Lcyt*b*. They found (DE)XXXL(LI)-type signal peptide, placed at 23 amino acids away from the *C*-terminal end, that targets the protein to the late endosome lysosomal membrane[40]. Further studies are required to evaluate the functional role of the C-terminal region of Dcyt*b*.

3-4-2 Structural comparison between Dcyt*b* and *At*Cytb_{561}

The structural environments of the two heme groups of Dcyt*b*, i.e., coordination of His residues to the irons and interaction with surroundings, are nearly identical to those of the heme groups occurring in *At*Cytb_{561} in terms of bis-histidyl coordination and interactions with surrounding residues. This is a common structural feature in the Cytb_{561} family. On the other hand, the structure of the protein intervening between the two heme groups that is expected to participate in intramolecular electron transfer differs significantly between Dcyt*b* and *At*Cytb_{561}. For both proteins, the shortest distance between the two heme centers is 15.5 Å. Inspection of the *At*Cytb_{561} structure led Lu and co-workers to propose involvement of a water molecule and F129 (located 3.5 and 3.6 Å from the cytoplasmic heme, respectively) (Figure 3-15b). Lu and co-workers suggested that the configuration of this water and the phenyl ring of F129 is suitable for electron transfer tunneling from the cytoplasmic heme to the non-cytoplasmic heme[26]. In addition to this through-space route, a through-bond route involving residues of transmembrane helix-2 was also suggested for *At*Cytb_{561} from computational analysis. However, no experimental investigation of the mechanism of electron transfer between the heme groups of *At*Cytb$_{561}$ has

been undertaken[26]. In the case of Dcyt*b*, putative electron transfer routes can be identified through main chain NH--OC interactions from the cytoplasmic heme ligand through six residues along helix α2 or α4, and, ultimately, the apical heme ligand (Figure 3-15a). Notably, the putative through-space pathway differs between Dcyt*b* and *At*Cytb_{561} in that (a) F129 of *At*Cytb_{561} corresponds to Y131 in Dcyt*b*, (b) no water molecule occurs in this pathway for Dcyt*b*, and (c) the phenyl group of Dcyt*b* residue F58 resides between Y131 and the heme while L59 occupies this position in *At*Cytb_{561} (Fig. 4). Consequently, Dcyt*b* residues F58 and Y131 could promote electron tunneling over a reasonable distance (3.6 to 4.9 Å) (Figure 3-15a). This is consistent with the *in vivo* Fe^{3+} reductase assay analysis of intramolecular electron transfer route of Dcyt*b* variants with substitutions at these positions (Figure 3-16b). The functional analysis revealed that these two residues are involved in Fe^{3+} reduction by mediating electron transfer. However, half of the activity still remains in these mutants, suggesting that in the absence of through space electron transfer, Dcyt*b* can still mediate Fe^{3+} reduction by through bond electron transfer. Which of these two routes is highly favorable has been considerable debate within the electron transfer modeling community. A research group lead by David N. Beratan reported an interesting idea about how electrons travel through proteins. Generally, electrons take the most common route to travel through series of covalent and hydrogen bonds, but sometimes the electron may leak from one chemical bond to a tunneling open space, strongly depending on the protein structure and external factors that causes structural change[41].

Comparison of the structures of Dcyt*b* and *At*Cytb_{561} also reveals that the apical surface of Dcyt*b* is far more negatively charged than that of the corresponding region of the plant enzyme. This characteristic is attributable to the presence of high number of negatively charged amino acid residues in Dcyt*b*, which are D188 (N186), E36 (G35), D41 (D42), E106 (K104), and E197 (E195) (the corresponding residues of the *At*Cytb_{561} enzyme are indicated in parentheses). This surface may assist in directing Fe^{3+} complexes toward the active site of the reductase to promote reaction.

The binding sites for ascorbate on the cytoplasmic sides of Dcyt*b* and *At*Cytb_{561} are identical and are defined by the conserved residues K79 (77), K83 (81) and R152 (150) (Figure 3-18a & b). This structural and functional conservation is not surprising as all members of the Cytb_{561} family employ ascorbate as a cytoplasmic electron donor. On the other hand, the ascorbate binding sites at the apical surface of the protein differ between Dcyt*b* and *At*Cytb_{561} in a manner that presumably reflects the differing structural requirements for Fe^{3+} reduction and monodehydroascorbate reduction (Figure 3-18c &d). The identification of the Zn^{2+} binding site on Dcyt*b* that is located adjacent to the apical binding site for ascorbate provides structural evidence for Cytb_{561} involvement in metal ion reduction. The cooperative binding of ascorbate and Zn^{2+} to the apical substrate binding site in the Dcyt*b* structure reveals key mechanistic insight into Dcyt*b* function. Other Cytb_{561} family members like *At*Cytb_{561}, are capable of reducing monodehydroascorbate to ascorbate at the expense of ascorbate, which binds to the cytoplasmic substrate binding site, to provide electron to monodehydroascorbate on the apical side. Dcyt*b* possesses an ascorbate binding site at the cytoplasmic surface of the protein as do other members of the Cytb_{561} family, but it also possesses an apical binding site for ascorbate that integrates a binding site for the Fe^{3+} substrate that could lead to formation of monodehydroascorbate upon reduction of Fe^{3+} to Fe^{2+}. The resulting monodehydroascorbate could then be reduced back to ascorbate by Dcyt*b*. This mechanism suggests that Dcyt*b* not only reduces Fe^{3+} but also regenerates ascorbate from monodehydroascorbate on the apical binding site using electrons provided by ascorbate at the cytoplasmic binding site.

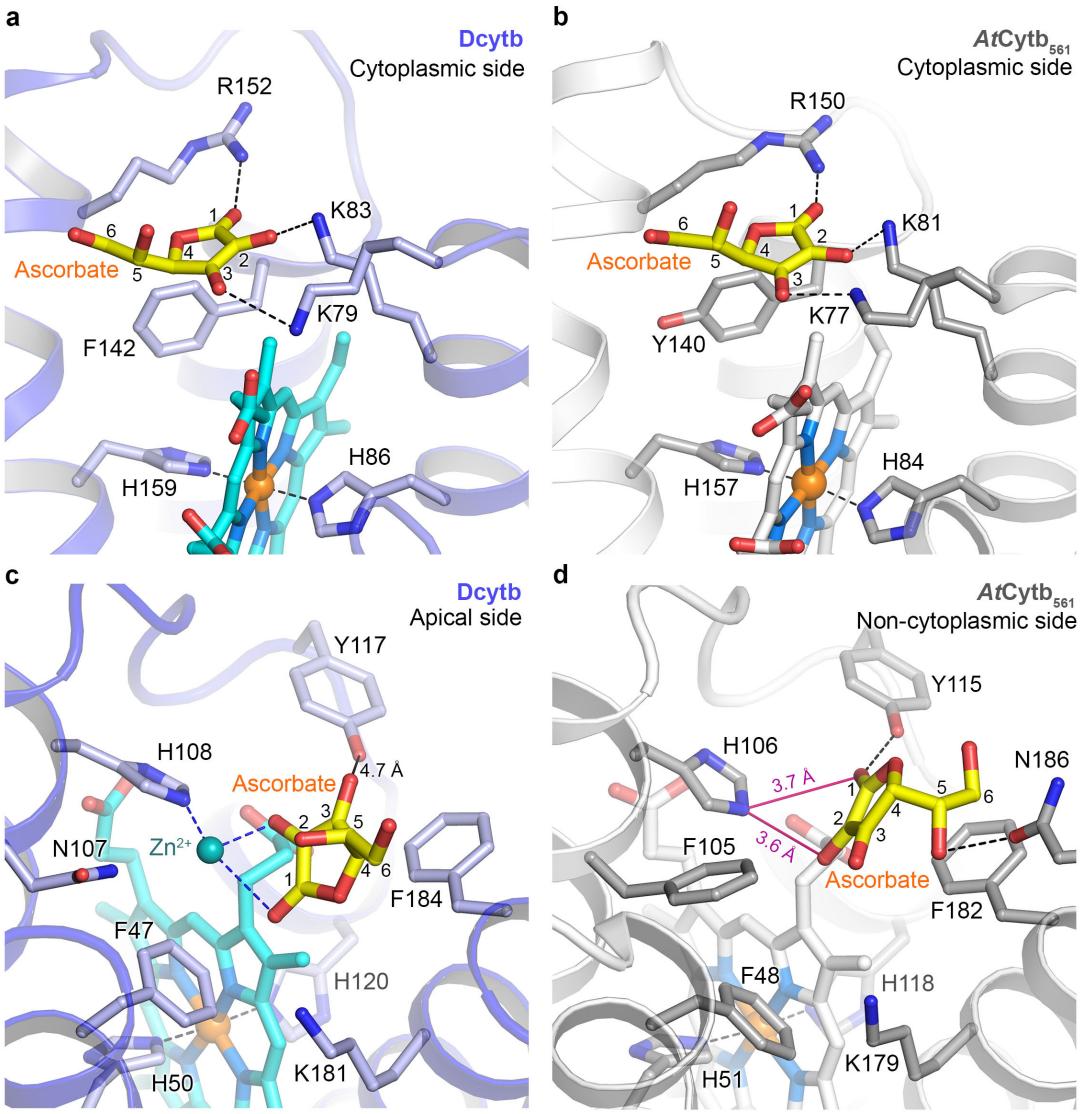

Figure 3-18. Comparison of the cytoplasmic and apical substrate-binding sites of Dcyt*b* and *At*Cyt*b*$_{561}$. a. Ascorbate is bound to the cytoplasmic side of Dcyt*b* by interaction with three conserved residues (K79, K83 and R152). F142 interacts with ascorbate by van der Waals contact. **b.** Similarly, ascorbate is bound to the cytoplasmic side of *At*Cyt*b*$_{561}$ by three conserved cationic residues, and Y140 replaces F142 of Dcyt*b*. **c.** Zn^{2+}-ascorbate is bound to the pocket on the apical side of Dcyt*b*. Zn^{2+} is coordinated by H108 and two-hydroxyl groups of ascorbate. H108 is conserved in all members of Cyt*b*$_{561}$. Ascorbate is in van der Waals contact with F184. The dihydroxyethyl moiety of ascorbate is free from interaction with the protein. **d.** Ascorbate is bound to the same site on the non-cytoplasmic side of *At*Cyt*b*$_{561}$. Ascorbate is in van der Waals contact with H106 and F182 and forms H-bonds with Y115 and N186.

H108, Y117, and N107 are all identified by the structure of Dcyt*b* as participating directly or indirectly in the binding of Zn^{2+} and, by implication, in the binding of Fe^{3+}. H108 plays a functionally conserved role in ascorbate binding at the apical surface of both Dcyt*b* and *At*Cyt*b*$_{561}$

and, in providing a ligand for Zn^{2+} binding, plays a direct role in the binding of this metal ion. Y117 is too distant (6.6 Å) from Zn^{2+} to serve as a ligand, and it is just beyond hydrogen-bonding distance from two ascorbate hydroxyl groups (4.7 Å). But the high affinity of a tyrosine phenolate for Fe^{3+} and the possible contribution of this residue to optimal orientation of bound ascorbate raise the possibility that Y117 might influence the Fe^{3+} reductase activity of this enzyme. Finally, the replacement of F105 in *At*Cyt*b*$_{561}$ by N107 in Dcyt*b* appears to create an open space for metal ion binding (Figure 3-18c & d). This is supported by Fe^{3+} reductase assay as shown in Figure 3-15b, where the Fe^{3+} reductase activity was significantly reduced by N107F mutant. Also, the Fe^{3+} reductase activity was more reduced when N107 was mutated by a larger phenylalanine residue, compared to the mutation by a smaller alanine residue. Superposition of the Dcyt*b* and *At*Cyt*b*$_{561}$ structures (Figure 3-19) suggests that the loop region between α5 and α6 also contributes to creation of this open space, which is of sufficient size to accommodate metal-chelator complex binding.

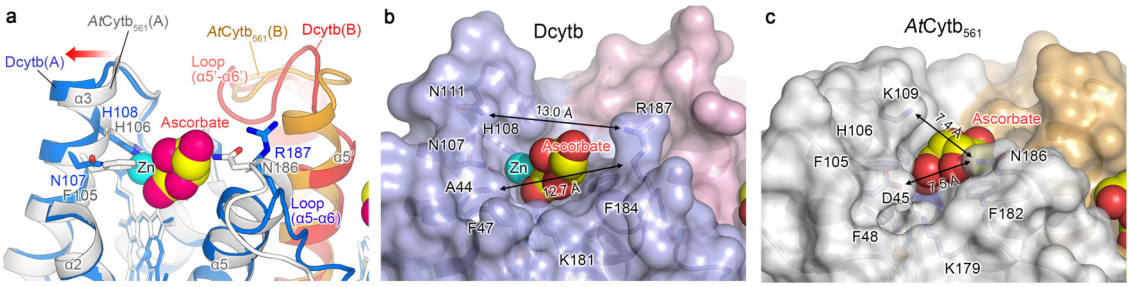

Figure 3-19. Comparison of the binding pockets on the apical surfaces of Dcyt*b* and *At*Cyt*b*$_{561}$. a. Superposition of Dcyt*b* and *At*Cyt*b*$_{561}$. The α3 helix is bent in the middle to accommodate binding of Zn^{2+} and ascorbate. The loop connecting α5–α6 contributes to this binding pocket and exhibits significant conformational difference between two proteins. Dcyt*b* (A-chain (blue), B-chain (red)) and *At*Cyt*b*$_{561}$ (A-chain (gray), B-chain (orange)) are colored as indicated. The A-chains of the two proteins were superimposed for calculations. Space filling models are shown for Zn^{2+} and ascorbate bound to Dcyt*b*. The α2 helices of the A-chains of both proteins are excluded from this view for clarity. **b.** The binding pocket of Dcyt*b* is wide and open. This view is same as shown in **a**. **c.** Ascorbate in the binding pocket of *At*Cyt*b*$_{561}$ is more buried.

Another significant finding in the present study is that ascorbate, citrate, and some organic acids can assist metal-binding to the apical side of Dcyt*b* as Fe^{3+}-chelators. Fe^{3+}-chelate is a common substrate for all known Fe^{3+} reductases (FRE and FRO proteins) reported so far.

However, the importance of this information has been overlooked due to the absence of supporting evidence. The present Dcyt*b* structure is the first to show the metal-chelator complex binding and emphasize the need of chelator for stable binding conformation of metal. The solubility and oxidization state of non-heme iron are highly affected by physiological pH. Both Fe^{3+} and Fe^{2+} are soluble at the low pH present in the stomach, but as pH increases upon passage into the duodenum, precipitates form unless iron is bound by soluble iron chelators[42]. Our functional assay with some dietary metal-chelators revealed that citric acid, malic acid, and oxalic acid promote Fe^{3+} reduction by Dcyt*b* at duodenal pH. Notably, although oxalate is a known inhibitor of iron uptake[43], it enhanced Fe^{3+} reduction by Dcyt*b* at both acidic and basic pH, so the inhibitory effect of oxalate on iron absorption is not the result of its effect on Fe^{3+} reduction. Interestingly, sugars such as glucose and fructose, which are found in oral iron supplements, have little or no effect on Dcyt*b* activity even though they are known to potentiate iron uptake[44,45]. These results support the conclusion that the Fe^{3+} binding site of Dcyt*b* is readily accessible to interaction with Fe^{3+}-chelator complexes. The pH dependent need of Fe^{3+}-chelator can also be observed by a notable difference between Dcyt*b* and Lcyt*b*, both of which are classified as Fe^{3+}-reductase. From the structure and functional analysis, it is known that N107 plays a crucial role in provide larger space for Fe^{3+}-chelator complex binding. However, this residue is replaced by phenylalanine in Lcyt*b*, similar to *At*Cytb_{561}. Since Lcyt*b* is expressed in lysosome, and the lysosomal pH is highly acidic, the Fe^{3+} remains soluble and therefore does not require chelator.

3-5 Conclusion

In summary, iron deficiency continues to be a significant cause of malnutrition in both developing and industrialized nations, in part because intestinal absorption of dietary iron is relatively inefficient. The current study provides structural insight into the function of one of the two duodenal proteins that are required for the uptake of dietary non-heme iron. It is also the first crystal structure that provide the metal binding information for a Cytb_{561} family member, which

differentiate their function as Fe^{3+}-chelate reductase or monodehydroascorbate reductase. In combination with the current biochemical studies, this work also provides structural insight into how ascorbate enhances iron uptake and how several potential iron ligands found in various foods promote or inhibit iron uptake. Understanding the importance and interaction between Fe^{3+}-chelator and Dcyt*b* could be useful in the development of new and effective therapeutic agents to promote iron uptake. Ultimately, knowledge of the structure of Dcyt*b* should enable development of new, structure-based strategies for promoting the reduction of dietary iron and thereby enhancing the bioavailability of this essential nutrient.

3-7 References

1. McKie, A. T., *et al.* An iron-regulated ferric reductase associated with the absorption of dietary iron. *Science* **291**, 1755-1759 (2001).

2. Gunshin, H., *et al.* Cloning and characterization of a mammalian proton-coupled metal-ion transporter. *Nature* **388**, 482-488 (1997).

3. Hentze, M. W., Muckenthaler, M. U., Galy, B. & Camaschella, C. Two to tango: Regulation of mammalian iron metabolism. *Cell* **142**, 24-38 (2010).

4. Lane, D. J., Bae, D. H., Merlot, A. M., Sahni, S. & Richardson, D. R. Duodenal cytochrome *b* (DCYTB) in iron metabolism: An update on function and regulation. *Nutrients* **7**, 2274-2296 (2015).

5. Takayama, S. J. & Mauk, A. G. The Cytochrome b_{561} Protein Family in *Handbook of Porphyrin Science: With Applications to Chemistry, Physics, Materials Science, Engineering, Biology and Medicine* (eds. Kadish, K. M., Smith, K. M., Guilard, R.) 339-370 (Singapore, 2012).

6. Anderson, G. J., *et al*. Ferric iron reduction and iron assimilation in *Saccharomyces cerevisiae*. *J. Inorg. Biochem.* **47**, 249-255 (1992).

7. Andrews, S. C., Robinson, A. K. & Rodriguez-Quinones, F. Bacterial iron homeostasis. *FEMS Microbiol. Rev.* **27**, 215-237 (2003).

8. Hell, R. & Stephan, U. W. Iron uptake, trafficking and homeostasis in plants. *Planta* **216**, 541-551 (2003).

9. Jain, A., Wilson, G. T. & Connolly, E. L. The diverse roles of FRO family metalloreductase in iron and copper homeostasis. *Front. Plant Sci.* **5**, 100 (2014).

10. Ohgami, R. S., *et al*. Identification of a ferrireductase required for efficient transferrin-dependent iron uptake in erythroid cells. *Nat. Genet.* **37**, 1264-1269 (2005).

11. Lane, D. J. & Richardson, D. R. The active role of vitamin C in mammalian iron metabolism: much more than just enhanced iron absorption. *Free Radic. Bio. Med.* **75**, 69-83 (2014).

12. Teucher, B., Olivares, M. & Cori, H. Enhancers of iron absorption: ascorbic acid and other organic acids. *Int. J. Vitam. Nutr. Res* **74**, 403-419 (2004).

13. Landau, E. M. & Rosenbusch, J. P. Lipidic cubic phases: A novel concept for the crystallization of membrane protein. *PNAS* **93(25)**, 14532-14535 (1996).

14. Caffrey, M. A comprehensive review of the lipidic cubic phase or *in meso* method for crystallizing membrane and soluble proteins and complexes. *Acta Crystallogr. F. Struct. Biol. Commun.* **71(Pt 1)**, 3-18 (2015).

15. Yamashita, K., Hirata, K. & Yamamoto, M. KAMO: towards automated data processing for microcrystals. *Acta Crystallogr. D Biol. Crystallogr.* **74**, 441-449 (2018).

16. Kabsch, W. Integration, scaling, space-group assignment and post-refinement. *Acta Crystallogr. D Biol. Crystallogr.* **66**, 133-144 (2010).

17. Foadi, J.*, et al.* Clustering procedures for the optimal selection of data sets from multiple crystals in macromolecular crystallography. *Acta Crystallogr. D Biol. Crystallogr.* **69**, 1617-1632 (2013).

18. McCoy, A. J.*, et al.* Phaser crystallographic software. *J. Appl. Crystallogr.* **40**, 658-674 (2007).

19. Adams, P. D.*, et al.* PHENIX: Acomprehensive Python-based system for macromolecular structure solution. *Acta Crystallogr. D Biol. Crystallogr.* **66**, 213-221 (2010).

20. Emsley, P. & Cowtan, K. Coot: Model-building tools for molecular graphics. *Acta Crystallogr. D Biol. Crystallogr.* **60**, 2126-2132 (2004).

21. Thorn, A. & Sheldrick, G. M. ANODE: Anomalous and heavy-atom density calculation. *J. Appl .Crystallogr.* **44**, 1285-1287 (2011).

22. Protchenko, O.*, et al.* Role of PUG1 in inducible porphyrin and heme transport in Saccharomyces cerevisiae. *Eukaryotic Cell* **7**, 859-871 (2008).

23. Dancis, A., Klausner, R. D., Hinnebusch, A. G. & Barriocanal, J. G. Genetic evidence that ferric reductase is required for iron uptake in *Saccharomyces cerevisiae*. *Mol. Cell. Biol.* **10**, 2294-2301 (1990).

24. Schneider, C. A., Rasband, W. S. & Eliceiri, K. W. NIH Image to ImageJ: 25 years of image analysis. *Nat. Methods* **9**, 671-675 (2012).

25. Oakhill, J. S., Marritt, S. J., Gareta, E. G., Cammack, R. & McKie, A. T. Functional characterization of human duodenal cytochrome *b* (Cybrd1): Redox properties in relation to iron and ascorbate metabolism. *Biochim. Biophys. Acta* **1777**, 260-268 (2008).

26. Lu, P.*, et al.* Structure and mechanism of a eukaryotic transmembrane ascorbate-dependent oxidoreductase. *Proc. Natl. Acad. Sci. U.S.A.* **111**, 1813-1818 (2014).

27. Conte, D., Narindrasorasak, S. & Sarkar, B. *In vivo* and i*n vitro* iron-replaced zinc finger generates free radicals and causes DNA damage. *J. Biol. Chem.* **271**, 5125-5130 (1996).

28. Dudev, T. & Lim, C. Competition among metal ions for protein binding sites: Determinants of metal ion selectivity in proteins. *Chem. Rev.* **114**, 538-556 (2014).

29. Holland, D. R., Hausrath, A. C., Juers, D. & Matthews, B. W. Structural analysis of zinc substitutions in the active site of thermolysin. *Protein Sci.* **4**, 1955-1965 (1995).

30. Sharp, K. H., Mewies, M., Moody, P. C. & Raven, E. L. Crystal structure of the ascorbate peroxidase–ascorbate complex. *Nat. Struct. Mol. Biol.* **10**, 303 (2003).

31. Hu, S., Smith, K. M. & Spiro, T. G. Assignment of protoheme resonance Raman spectrum by heme labeling in myoglobin. *J. Am. Chem. Soc.* **118**, 12638-12646 (1996).

32. Humphrey, W., Dalke, A. & Schulten, K. VMD: visual molecular dynamics. *J. Mol. Graph* **14**, 33-38, 27-38 (1996).

33. Balabin, I. A., Hu, X. & Beratan, D. N. Exploring biological electron transfer pathway dynamics with the Pathways plugin for VMD. *J. Comput. Chem.* **33**, 906-910 (2012).

34. Bleeg, H. S. & Christensen, F. Biosynthesis of ascorbate in yeast. Purification of L-galactono-1,4-lactone oxidase with properties different from mammalian L-gulonolactone oxidase. *Eur. J. Biochem.* **127**, 391-396 (1982).

35. Fallingborg, J.*, et al.* pH-profile and regional transit times of the normal gut measured by a radiotelemetry device. *Aliment. Pharmacol. Ther.* **3**, 605-613 (1989).

36. Zhang, H., Onning, G., Oste, R., Gramatkovski, E. & Hulthen, L. Improved iron bioavailability in an oat-based beverage: the combined effect of citric acid addition, dephytinization and iron supplementation. *Eur. J. Nutr.* **46**, 95-102 (2007).

37. Liu, W., *et al.* Purification and characterization of bovine adrenal cytochrome b_{561} expressed in insect and yeast cell systems. *Protein Expr. Purif.* **40**, 429-439 (2005).

38. Su, D. & Asard, H. Three mammalian cytochromes b_{561} are ascorbate-dependent ferrireductases. *FEBS J.* **273**, 3722-3734 (2006).

39. Glanfield, A., *et al*. A Cytochrome b_{561} with ferric reductase activity from the parasitic blood fluke, *Schistosoma japonicum*. *PLOS Negl. Trop. Dis.* **4(11)**, e884 (2010).

40. Zhang, D. L., Su, D., Berczi, A., Vargas, A. & Asard, H. An ascorbate-reducible cytochrome b_{561} is localized in macrophage lysosomes. *Biochim. Biophys. Acta* **1760**, 1903-1913 (2006).

41. Prytkova, T. R., Kurnikov, I. V. & Beratan, D. N. Coupling coherence distinguishes structure sensitivity in protein electron transfer. *Science* **315**, 622-625 (2007).

42. Dokkum, W. V. Significance of iron bioavailability for iron recommendations. *Biol. Trace Elem. Res.* **35**, 1-11 (1992).

43. Gillooly, M., *et al.* The effects of organic acids, phytates and polyphenols on the absorption of iron from vegetables. *Br. J. Nutr.* **49**, 331-342 (1983).

44. Christides, T. & Sharp, P. Sugars increase non-heme iron bioavailability in human epithelial intestinal and liver cells. *PLoS One* **8**, e83031 (2013).

45. Garcia-Casal, M. N., *et al.* Iron absorption from elemental iron-fortified corn flakes in humans. Role of vitamins A and C. *Nutr. Res.* **23**, 451-463 (2003).

Chapter 4 : The role of Dcyt*b* and DMT-1 in regulating non-heme iron absorption

4-1 Introduction

DMT-1, also known as Natural Resistance-Associated Macrophage Protein 2 (NRAMP 2), Divalent Cation Transporter-1 (DCT-1) or Solute Carrier Family 11 Member 2 (SCL11A2), is an active divalent metal transporter found in all kingdoms of life, with a high degree of sequence conservation[1]. In human, the expression of DMT-1 in duodenal enterocyte was first reported by Gunshin *et al.*, in 1997[2]. They showed that DMT-1 can transport various divalent metals (Fe^{2+}, Zn^{2+}, Cd^{2+}, Mn^{2+}, Cu^{2+}, Co^{2+}, Ni^{2+}, Pb^{2+}), and is highly expressed in duodenum, followed by a slightly lesser expression in kidney and a small amount of expression in brain. They also showed the increase in DMT-1 expression in duodenum, in iron deficient diet. Following this discovery, many studies have been conducted on DMT-1 to evaluate its structure and mechanism of metal transport.

For an efficient absorption of non-heme iron from diet, the cooperative involvement of both Dcyt*b* and DMT-1 is required. Fe^{3+} iron from diet is first reduced by dcyt*b* before being transported into the duodenal enterocyte by DMT-1. The fe^{2+} is then captured by PCBP-2, carried to ferroportin, transported into the blood vessel, oxidized back to ferric by hephaestin, and carried to other parts of cells in transferrin bound form. A missing piece of information here, is how the reduced Fe^{2+} is transported from Dcyt*b* to DMT-1 (Figure 4-1). This information is important as it determines the amount of iron absorbed from diet. In order to propose some hypothesis, the structural properties of DMT-1 and Dcyt*b* was studied in detail.

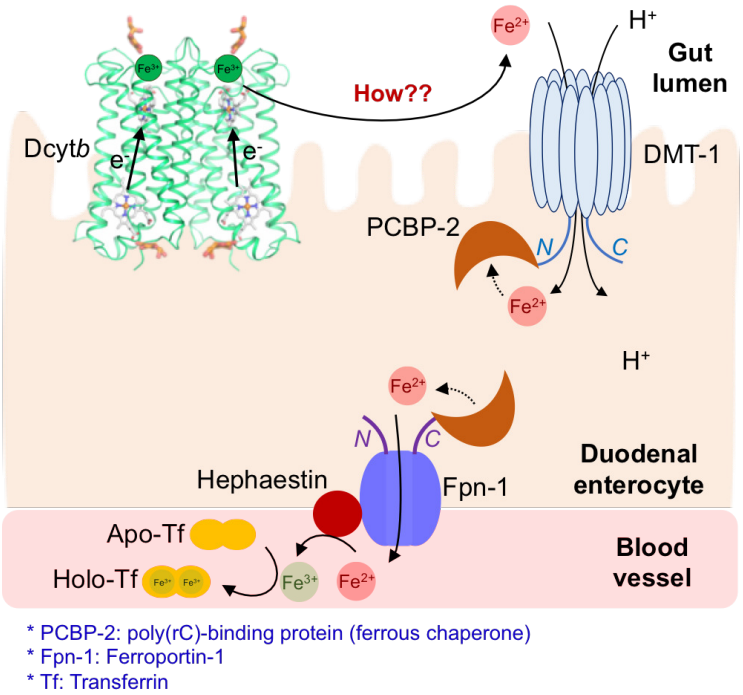

Figure 4-1. Schematic representation of iron transport from gut lumen to the blood vessel. The route of iron transport from gut lumen to blood vessel is well understood by regulatory role of various proteins, which includes DMT-1, PCBP-2, Fpn-1 and Tf. However, the question on how the reduced Fe^{2+} is transported from Dcyt*b* to DMT-1 is yet to be solved.

4-1-1 Structural analysis of DMT-1

DMT-1 is generally known to have 12 transmembrane domains, and like Dcyt*b*, both its *N*- and *C*-terminal regions are placed on the cytoplasmic side. So far, two crystal structure of DMT-1 have been reported. The first structure is from *Staphylococcus capitis*, was reported by Ehrnstorfer *et al*., in 2014. In this report, they showed the metal binding site in DMT-1, and found that the amino acids involved in the metal binding are conserved in human DMT-1. This binding site is known to be conserved among all family members of DMT-1 regardless of species[1]. Consequently, this group reported another crystal structure of DMT-1 from *Eremococcus coleocola*, in 2017. On contrary to the previously reported structure, the outward facing conformation of DMT-1 was reported in this study. They showed proton-coupled transition metal transport by DMT-1 using structural and functional study[3]. Based on these reported structures, the metal binding side and the transport mechanism are probably conserved in human DMT-1.

Indeed, sequence alignment between these three proteins showed that the bacterial DMT-1 shared 30 to 37% identity to human DMT-1. However, a huge difference was observed from the sequence alignment, where the human DMT-1 has relatively long *N*- and *C*-terminal sequence (Figure 4-2). Since this feature is very specific to human, solving the structure of human DMT-1 might give us new insights into this protein's function.

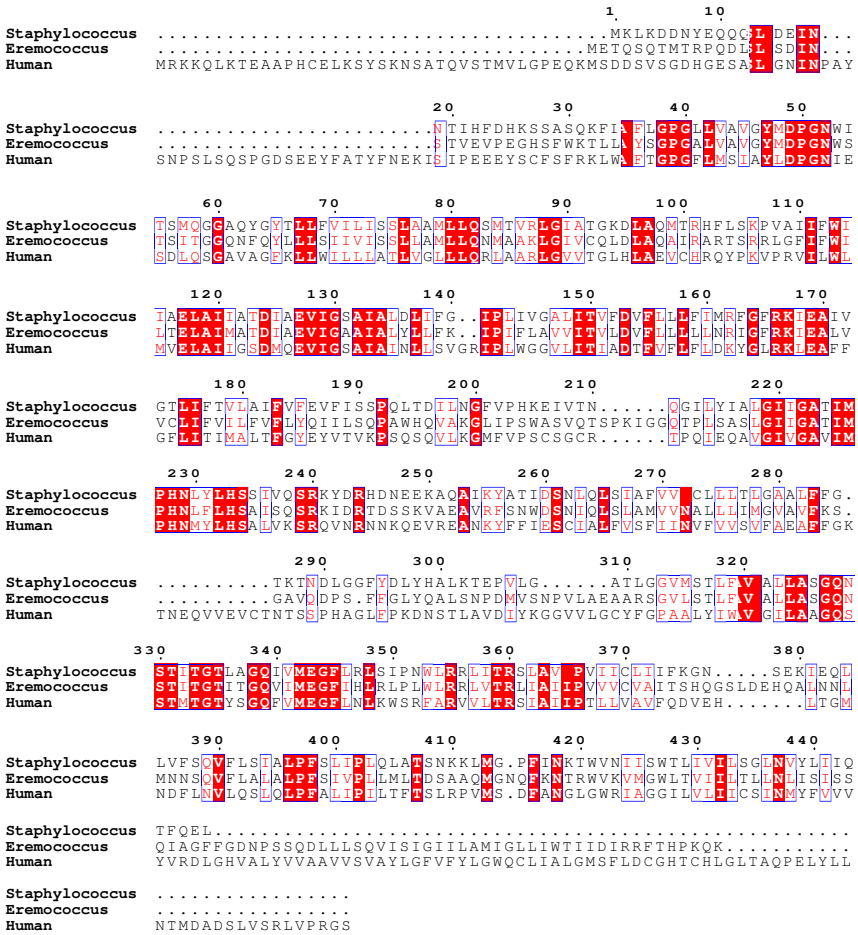

Figure 4-2. Sequence alignment of DMT-1 from bacteria and human. DMT-1 from *Staphylococcus capitis*, *Eremococcus coleocola* and human are aligned. Residues conserved in all three sequences are highlighted in red. Human DMT-1 has a *N*- and *C*-terminal sequence that is longer than bacterial DMT-1

The lengthy *N*- and *C*-terminal sequence of DMT-1 classify this protein into four isoforms, that are characterized by two transcripts at both terminals (Figure 4-3). Two alternative transcripts identified on the *C*-terminal, known as +IRE and -IRE, which means with and without iron responsive element (IRE). IRE mediates controlled expression of DMT-1 under iron deficiency,

by binding to iron regulatory proteins (IRPs). Another two additional transcripts were identified on the *N*-terminal, one mRNA transcript starts in exon 1A, skips the next exon (1B), and splices directly with exon 2, and another mRNA transcript, skips exon 1A, starts in exon 1B and splices with exon 2.

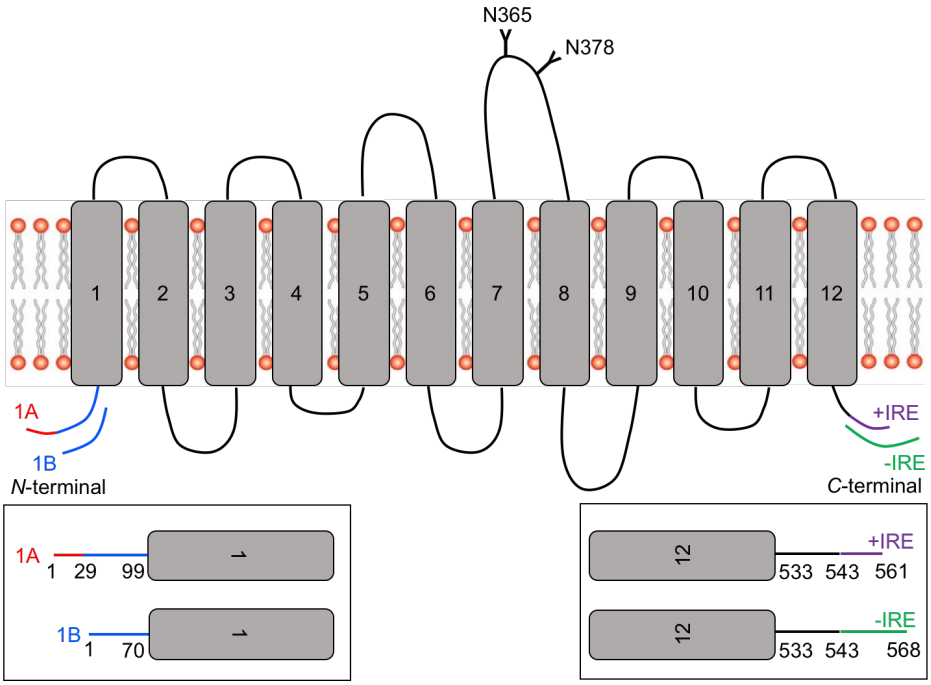

Figure 4-3. Schematic representation of four DMT-1 isoform. DMT-1 consists of 12 transmembrane helices, with differing lengths of *N*- and *C*-terminals regions, that characterize this protein into four isoforms. The *N*- and *C*- terminal region are expanded and the number of amino acid residues are shown. As shown in the diagram, the *N*-terminal region of DMT-1 can either possess only exon 1B (blue) or both exon 1A (red) and 1B (blue). On the *C*-terminal end, amino acid residues are conserved from 533 to 543, and differs in sequence and length thereafter for DMT-1 with (purple) and without (green) the iron responsive element (IRE).

The exclusive *N*-terminal peptide sequence encoded by exon 1A contains extra 29 amino acids on the upstream of 1B, that contains the signal sequence, Leu16, that has the role as a retention signal for plasma membrane. In addition to these, this isoform contains 2 *N*-linked glycosylation sites, N365 and N378, that play a critical role in targeting the protein to the apical membrane[4] (Figure 4-3). Based on these known properties, the four isoforms of human DMT-1 are listed as follow, 1A/(+IRE), 1A/(−IRE), 1B/(+IRE), and 1B/(−IRE)[5]. Out of these four isoforms, 1A/(+IRE) is tissue specific, and is highly expressed in duodenum and caco-2 cells.

In addition to aiding in categorizing the isoforms, the cytoplasmic loop of DMT-1 plays a crucial role in regulating the non-heme iron transport from gut lumen into duodenal enterocyte. The Fe^{2+}-transport is initiated only when the *N*-terminal region of DMT-1 interacts with PCBP-2, a Fe^{2+} chaperone. Following that, there is possibility that this cytoplasmic loop is also involved in regulating the transport of reduced Fe^{2+} from Dcyt*b* to DMT-1. In order to propose some interaction site between Dcyt*b* and DMT-1, the structural properties of Dcyt*b* was analyzed in detail.

4-1-2 Structural summary of Dcyt*b*

The current structure of Dcyt*b* provides extensive knowledge on the individual Fe^{3+} reduction function by Dcyt*b*, in terms of the substrate binding and electron transfer. However, around 56 amino acid residues at the *C*-terminal region are absent in this structure because the electron density map was highly disordered. Some reports on single nucleotide polymorphisms (SNPs) linked with hereditary hemochromatosis showed mutations of two amino acids residues, R226H and S266N (Figure 4-4) around this *C*-terminal region[6, 7]. The position of these mutants increase the curiosity about the role of this region in regulating iron absorption.

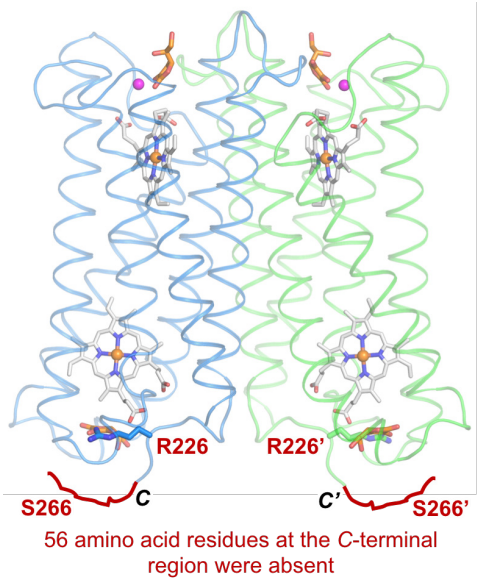

Figure 4-4. SNPs in Dcyt*b* that are linked to hereditary hemochromatosis. Two amino acid residues, R226 and S266, around the *C*-terminal region are mutated as a result of this polymorphism.

The possible role of this region in localization has already been discussed in section 3-4-1 by comparison with other human cytochrome b_{561} family members. In addition to this, like DMT-1, the cytoplasmic loop of Dcyt*b* might also have regulatory role for controlled non-heme iron absorption. For instance, this region may contain ubiquitination site like ferroportin-1. Ferroportin-1 contains ubiquitination site on its cytoplasmic loop, which is the binding site of *N*-terminal of hepcidin. When iron level is elevated in human body, this regulation system is activated to prevent iron overload[9]. In addition to this, this cytoplasmic loop of Dcyt*b* might also interact with other related proteins like DMT-1 for the regulation of controlled non-heme iron absorption from diet. This possibility will be further discussed in the next section.

4-1-3 Interaction between Dcyt*b* and DMT-1

A critical factor needed to initiate a substrate transfer from one protein to another is the signal between two involved proteins. One way this signal is formed is via interaction between the respective proteins. For instance, Fe^{2+} transport from DMT-1 to PCBP-2 is induced by the interaction between PCBP-2 and *N*-terminal of DMT-1, and Fe^{2+} transport from PCBP-2 to ferroportin-1 is induced by the interaction between PCBP-2 and *C*-terminal of ferroportin-1. Similarly, Fe^{2+} transport from Dcyt*b* to DMT-1 probably mediated by the interaction between these two proteins (Figure 4-5). However, an interesting issue is where does the interaction occurs. Both previous examples show interaction between soluble protein and membrane protein. However, Dcyt*b* and DMT-1 are both membrane proteins and to date there is no significant evidence to prove or disprove the complex of these two proteins. Interaction might occur either directly between the *C*-terminal of Dcyt*b* and *N*-terminal of DMT-1, or indirectly mediated by the known interacting protein, PCBP-2. In order to test this hypothesis the structural properties of DMT-1 with and without PCBP-2 need to be studied.

4-1-4 Existence of a Fe^{2+}-chelator in the gut lumen

Structural studies of Dcyt*b* also revealed an important role of dietary iron chelators in transporting Fe^{3+} to the binding pocket on the apical surface of Dcyt*b*. This finding shows that free iron in our body always requires chelator or carrier to be transported elsewhere. For instance, Fe^{2+} in duodenal cytoplasm is chelated by PCBP-2 and Fe^{3+} in blood plasma is carried by transferrin. However, to date, there's no information available on the existence of Fe^{2+} chelator in the lumen of duodenum. One possibility is that, after Fe^{3+} reduction by Dcyt*b*, Fe^{2+} is continuously chelated by ascorbate to prevent Fe^{2+} oxidation[10], and is carried to DMT-1. Upon binding of Fe^{2+}-ascorbate complex to DMT-1, Fe^{2+} is released and transported into duodenal enterocyte. This hypothesis can be tested by functional studies to check affinity between ascorbate and DMT-1, or by structural studies by solving the complex structure of DMT-1 with Fe^{2+}-ascorbate, to check if there is any possible binding site.

The two proposed options that might be responsible for the transfer of the reduced Fe^{2+} from Dcyt*b* and DMT-1 are summarized in Figure 4-5.

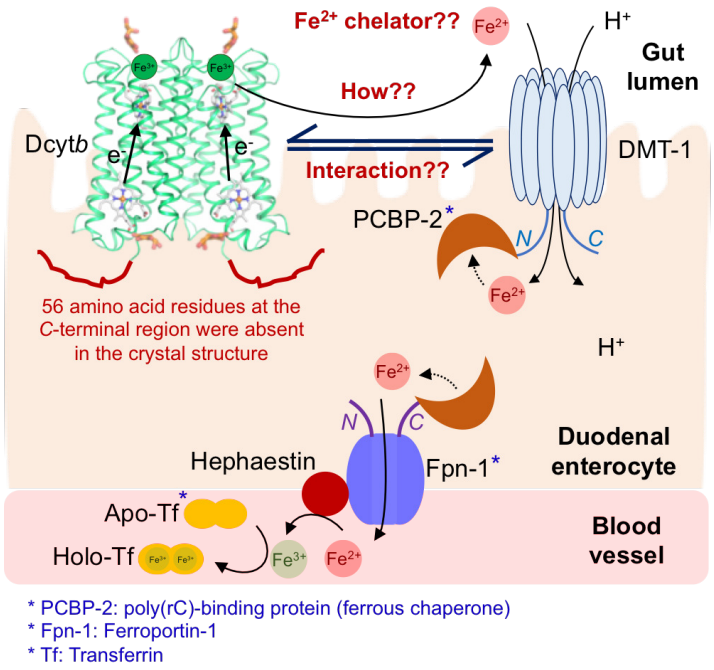

Figure 4-5. Schematic representation of iron transport from gut lumen to the blood vessel. Fe^{2+} reduced by Dcyt*b* is carried to DMT-1 by either or both Fe^{2+} chelator and possible interaction between Dcyt*b* and DMT-1.

Clearly, more research is needed to test both these hypotheses. As an initial approach to that, the structural and functional properties of DMT-1 is currently being studied. The objective of my future plans is to understand the structural feature of 1A/(+IRE) isoform. This isoform contains the signal sequence on its *N*-terminal that interact with iron chaperone PCBP2 for subcellular distribution of Fe^{2+}, and also probably contains the signal sequence that interact with Dcyt*b* to trigger or terminate the Fe^{2+} transport from gut lumen into duodenal enterocyte. Following that, the proposed experiments are as follow:

1) Establish the expression and purification protocol for 1A/(+IRE) DMT-1 isoform.
2) Crystallization of DMT-1 by vapor diffusion and LCP techniques.
3) Co-crystallization of DMT-1 with the known interacting protein, PCBP-2, to see the protein interacting side. Probably the interacting side of DMT-1 to Dcyt*b* is the same as PCBP2. In that case, this information could be used for site directed mutagenesis studies and *in vivo* functional assay.

This coming research will provide understanding about the structural and functional features of 1A/(+IRE) DMT-1 isoform, which can provide answers to many unsolved questions on controlled iron absorption in human.

4-2 Preliminary purification of DMT-1

4-2-1 Material and methods

4-2-1-1 Expression of DMT-1

Artificially synthesized (Biomatik), codon optimized human DMT-1 gene (isoform 1A/(+IRE)) that includes *C*-terminal His-tag was cloned into pPIC9K vector (Invitrogen) for expression in *Pichia pastoris*. Preculture was grown in 5 mL BMGY medium overnight at 30°C with constant stirring at 180 rpm. Cells harvested from preculture was washed and resuspended with 5 mL of sterilized water. This cell was used for the main culture (75 mL of BMY medium

containing 1% (w/v) yeast extract, 2% (w/v) peptone, 0.1 M potassium phosphate buffer, 1.34% (w/v) yeast nitrogen base, 0.002% (w/v) biotin and 0.5% methanol) to a final OD_{600} of 0.5. The cells were grown at 30°C with constant stirring at 180 rpm for 24 hours. The culture was supplemented with another 0.5% methanol, further grown for 6 more hours and harvested. The harvested cells (~ 4 g) were resuspended in 40 mL lysis buffer containing 50 mM potassium phosphate buffer (pH 7.6), 150 mM NaCl and one tablet of cOmplete EDTA-free protease inhibitor cocktail (Roche), followed by disruption by vortexing with zirconia beads (equal volume with lysis buffer) for 8 min ((1 min disruption +5 min interval on ice) – repeat 8 times). Cell debris was removed by centrifugation (10,000 × *g* for 20 min). The supernatant fluid was collected and sedimented by ultracentrifugation (40,000 × *g* for 1 h) to obtain the membrane fraction. Membrane fraction was then homogenized with lysis buffer.

4-2-1-2 Purification of DMT-1

The membrane fraction (~ 0.25 g) was homogenized in solubilization buffer (Na_2HPO_4 (50 mM), citric acid (10 mM) and NaCl (150 mM), pH 5.8). The membrane concentration was measured by bicinchoninic acid assay (BCA assay), and final concentration of membrane was adjusted ~7 mg/mL before solubilization of the membrane with 1% (w/v) DDM for 1 h at 4°C. Following ultracentrifugation (40,000 rpm for 1 h), the supernatant fluid was loaded onto a column of Ni^{2+}-nitrilotriacetate affinity resin (Ni-NTA; Qiagen). Non-specifically bound material was eluted from this column with lysis buffer containing 10 mM imidazole (pH 5.8) (washing buffer), and the solubilized DMT-1 was eluted by stepwise elution using the same buffer containing 100, 300 and 500 mM imidazole (pH 5.8).

4-2-2 Results

4-2-2-1 Purification of DMT-1

Recombinant human DMT-1 was overexpressed in *Pichia pastoris* and purified by nickel-affinity (Figure 4-6). DMT-1 can be successfully purified by affinity chromatography, However, based on the SDS-PAGE analysis, high purity is not achieved by this single step purification. Further optimization to obtain protein with high purity for crystallization trials will be performed in near future. As an initial approach, the protein purity will be improved by gel filtration chromatography.

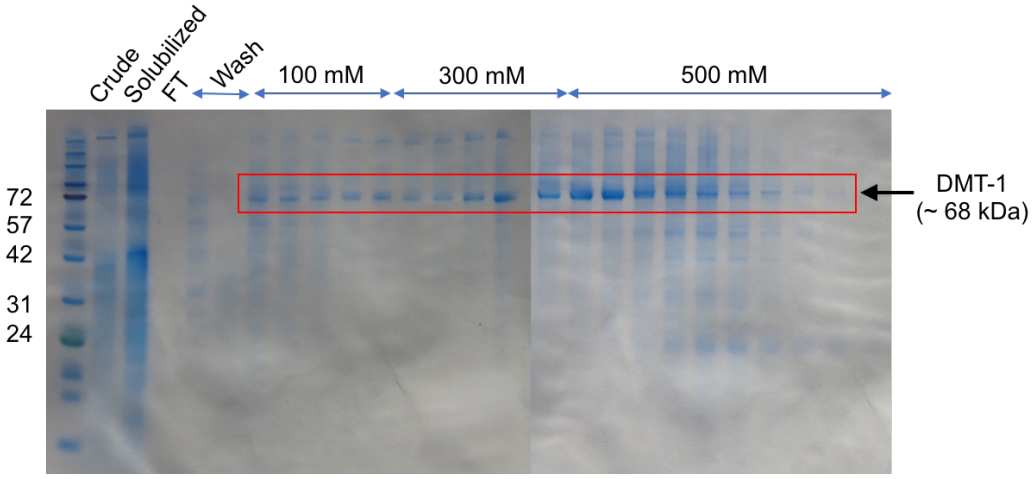

Figure 4-6. Preliminary purification profile of DMT-1. DMT-1 was purified by affinity chromatography using Ni-NTA column. The protein was eluted by stepwise elution using 100, 300 and 500 mM imidazole.

4-3 References

1. Ehrnstorfer, I. A., Geertsma, E. R., Pardon, E., Stegaert, J. & Dutzler, R. Crystal structure of a SLC11 (NRAMP) transporter reveals the basis for transition-metal iron transport. *Nat. Struct. Mol. Biol.* **21**, 990-996 (2014).

2. Gunshin, H., *et al.* Cloning and characterization of a mammalian proton-coupled metal-ion transporter. *Nature* **388**, 482-488 (1997).

3. Ehrnstorfer, I. A., Manatschal, C., Arnold, F. M., Laederach, J. & Dutzler, R. Structural and mechanistic basis of proton-coupled metal ion transport in the SLC11/NRAMP family. *Nat. Comm.* **8**, 14033 (2017).

4. Yanatori, I. & Kishi, F. DMT-1 and iron transport. *Free Radic. Biol. Med.* In press (2018).

5. Skjørringe, T., Burkhart, A., Johnsen, K. B. & Moos, T. Divalent metal transporter 1 (DMT1) in the brain: implications for a role in iron transport at the blood-brain barrier, and neuronal and glial pathology. *Front. Mol. Neurosci.* **8**, 1-13 (2015).

6. Zaahl, M. G., *et al*. Analysis of genes implicated in iron regulation in individuals presenting with iron overload. *Hum. Genet.* **115**, 409-417 (2004).

7. McKie, A. T., *et al*. An iron-regulated ferric reductase associated with the absorption of dietary iron. *Science* **291**, 1755-1759 (2001).

8. Yanatori, I., Yasui, Y., Tabuchi, M. & Kishi, F. Chaperone protein involved in transmembrane transport of iron. *Biochem. J.* **462**, 25-37 (2014).

9. Drakesmith, H., Nemeth, E. & Ganz, T. Ironing out ferroportin. *Cell Metab.* **22**, 777-787 (2015).

10. Plug, C. M., Dekker, D. & Bult, A. Complex stability of ferrous ascorbate in aqueous solution and its significance for iron absorption. *Int. J. Clin. Pharm.* **6**, 245-248 (1984).

Chapter 5: General conclusion

Deficiency or over exposure to iron has been known to cause noticeable effects to human. Studies are being continuously conducted to understand the role of various proteins involved in maintaining the complex iron homeostasis in human, to find solutions to this extensively spreading iron imbalance diseases. In the current study, attempt was made to explain the role of three important membrane proteins, *Ce*HRG-4, Dcyt*b* and DMT-1, involved in the regulation of systemic iron homeostasis.

In the first part of this study (Figure 5-1), the role of heme transport by *Ce*HRG-4 has been functionally proved. However, the transport mechanism remains unsolved due to the challenges in crystallization and atomic level structural determination. Crystallization of *Ce*HRG-4 by LCP technique to provide a native like environment for the crystal packing is the nearest future plan that can be performed for this project.

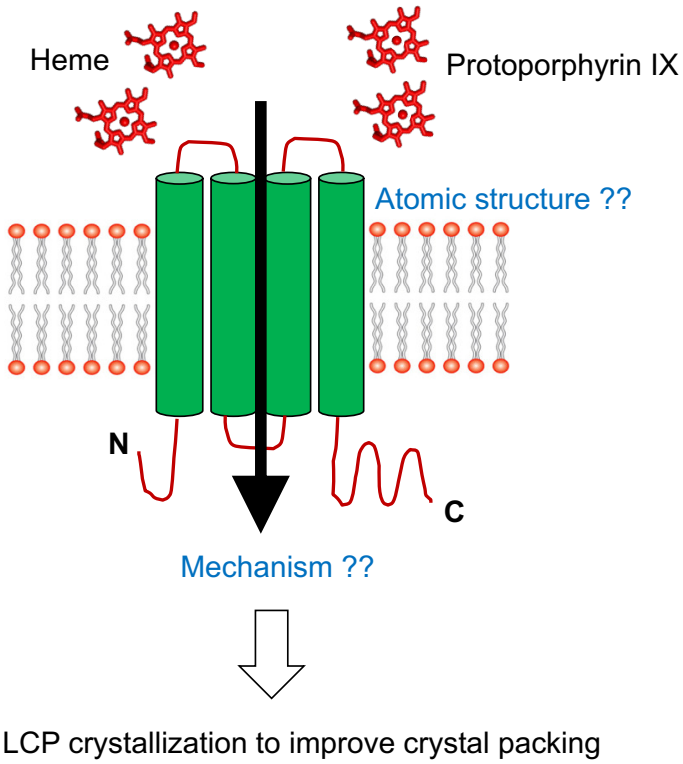

Figure 5-1. Summary of *Ce*HRG-4 study. The role of *Ce*HRG-4 in the transport heme and porphyrin ring is known from functional assay. However, the mechanism of heme transport remains unsolved due to the challenges in crystallization.

In the second part of this study, the role of Dcyt*b* and DMT-1 in non-heme iron absorption was studied. This study summarizes some important structural aspects of Dcyt*b*, in terms of substrate binding and electron transfer route. This is the first reported structure that shows the metal binding site for a cytochrome b_{561} family member. This is also the first structure that emphasize the importance of chelators in increasing Fe^{3+} solubility and binding stability, which in turn enhances the ferric reductase activity. Nevertheless, the C-terminal end loop region could not be modelled in the current structure (Figure 5-2). Based on some reported polymorphisms in Dcyt*b*, this region is probably involved in the regulatory role of iron absorption to control iron related diseases like iron overload. The study to analyse the possible role of this C-terminal region in iron regulation through interaction with other related proteins like DMT-1 is currently on-going. This hopefully provides a better understanding to address iron related diseases like iron deficiency anemia and hereditary hemochromatosis.

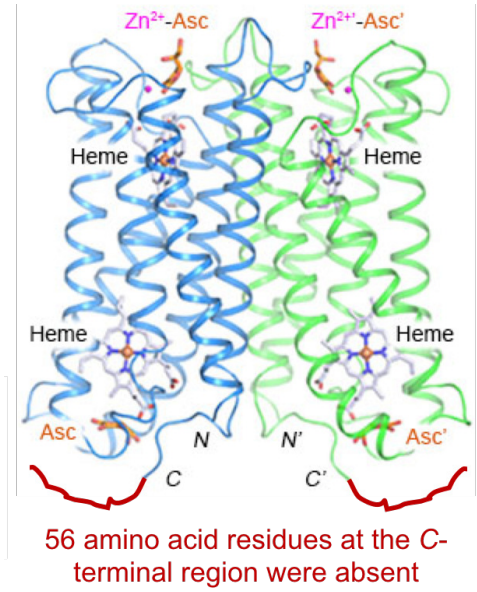

Figure 5-2. Summary of structural analysis of Dcyt*b*. The current structure provides information on the mechanism of Fe^{3+} reduction by Dcyt*b* and the importance of dietary iron chelators in mediating Fe^{3+} reduction.

Acknowledgements

Firstly, I would like to express my sincere gratitude to my supervisor, Professor Yoshitsugu Shiro, for his endless guidance and suggestions throughout my Ph.D. Next, I would like to thank my co-supervisor Dr. Hitomi Sawai, Assistant Professor in University of Hyogo, for her patience, encouragement, guidance and suggestions in my research. I would also like to thank Dr. Hiroshi Sugimoto, Senior Research Scientist, RIKEN SPring-8 Center for his advice and support for my study.

I am much obliged to my thesis committee members, Professors Masao Sakaguchi and Yoshiki Higuchi for their time and assistance during my Ph.D evaluations. I would also like to thank my external committee members, Professors Koichiro Ishimori (Hokkaido University) and Svetlana V. Antonyuk (University of Liverpool) for their advice in thesis preparation.

The thesis work has been done with the support of many people and I am grateful to all my group members, including Dr. Hiromi Togashi, Dr. Takehiko Tosha, Ms. Hanae Takeda and Ms. Honami Asakura. I would also like to thank Professor Kouhei Tsumoto and Dr. Satoru Nagatoishi (University of Tokyo) for helping me to conduct ITC experiments in their laboratory, Professor Takashi Ogura, University of Hyogo for allowing me to use your Raman equipment, beamline scientists Drs. Keitaro Yamashita and Kunio Hirata of SPring-8 for your assistance in the data collection, Dr. Shin-ichi J. Takayama for his advice on preparation of the protein sample of Dcyt*b*, Drs. Tomohiro Nishizawa (University of Tokyo) and Tatsuro Shimamura (Kyoto University) for their advice on LCP crystallization, Dr. Ilya A. Balabin for his help with the *Pathways* plugin, Professor Iqbal Hamza and Dr Xiaojing Yuan (University of Maryland) for their support and advice in yeast constructs and functional studies for CeHRG-4 and Dcyt*b* projects and Professor A. grant Mauk for his advice in manuscript preparation for Dcyt*b* project.

I would like to acknowledge the Leading Program in Doctoral Education of Graduate School of Life Science, University of Hyogo for the outstanding educational curriculum, funding

and financial support. I like to express my deep gratitude to the Picobiology staffs and my friends for helping me not only to the academic but also in my personal life in Japan. I would also like to thank my lab members with whom I spent this four and half years, you all are very kind, polite and helpful. Finally, a special thanks to all my family and friends for their boundless prayers and sacrifice for my success. Thank you all!

平成 2018 年 12 月 07 日

Menega Ganasen